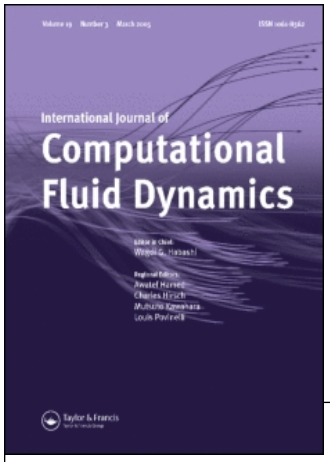

International Journal of Computational Fluid Dynamics
Publication details, including instructions for authors and subscription information:
http://www.informaworld.com/smpp/title~content=t713455064

Comparison of solution accuracy of multidimensional residual distribution and Godunov-type finite-volume methods

S. M. J. Guzik [a]; C. P. T. Groth [a]
[a] Institute for Aerospace Studies, University of Toronto, Toronto, ON, Canada

Online Publication Date: 01 January 2008

To cite this Article: Guzik, S. M. J. and Groth, C. P. T. (2008) 'Comparison of solution accuracy of multidimensional residual distribution and Godunov-type finite-volume methods', International Journal of Computational Fluid Dynamics, 22:1, 61 — 83

To link to this article: DOI: 10.1080/10618560701748176
URL: http://dx.doi.org/10.1080/10618560701748176

International Journal of Computational Fluid Dynamics
Vol. 22, Nos. 1–2, January–February 2008, 61–83

Taylor & Francis
Taylor & Francis Group

Comparison of solution accuracy of multidimensional residual distribution and Godunov-type finite-volume methods

S.M.J. Guzik and C.P.T. Groth*

Institute for Aerospace Studies, University of Toronto, 4925 Dufferin Street, Toronto, ON, Canada M3H 5T6

(*Received January 2007; final version received 11 June 2007*)

While it is apparent that residual distribution (RD) methods generally offer higher accuracy than finite volume (FV) methods on similar meshes, few studies have directly compared the performance of the two approaches in a systematic and quantitative manner. In this study, solutions are obtained for scalar equations and the Euler equations governing two-dimensional inviscid compressible gaseous flows. Comparisons between RD and FV are made for smooth and discontinuous flows solved on structured quadrilateral meshes. Since the RD method is applied on simplexes, the effect of tessellating the quadrilaterals into triangles by aligning the diagonal with the characteristic vectors is explored. The accuracy of the spatial discretisation is assessed by examining the L_1-error norm of a given quantity and its dependence on the grid size. For the Euler equations, two methods of distributing the system are used: system decomposition and matrix distribution. The results indicate that RD schemes can indeed surpass FV schemes in terms of solution accuracy. However, it is also shown that standard non-linear RD schemes can suffer from a degradation in accuracy to the extent that they can become even less accurate than FV methods. Furthermore, numerical difficulties were encountered in some solutions obtained with the RD schemes, particularly for the case of steady subsonic flow around a circular cylinder.

Keywords: residual distribution; finite volume; fluctuation splitting; Euler equations

1. Introduction

Research into residual distribution (RD) methods is stimulated by a desire to improve the accuracy of multidimensional solutions to hyperbolic partial differential equations. This field of research was initiated because of a dissatisfaction with current finite volume (FV) methods. While elegant and physical in one dimension, FV methods do not extend readily to multiple dimensions because the Riemann problem itself does not extend readily to multiple dimensions. The usual workaround is to apply the one dimensional scheme in multiple directions, a process in which the splitting of the flux becomes biased in directions normal to the faces of the computational cells. Consequently, the schemes are no longer quite as physical and this causes a corresponding decrease in the accuracy via excess numerical dissipation. As shown by Roe and Sidilkover (1992), dimensional splitting is about the worst thing one can do for first-order solutions. RD methods attempt to correct this deficiency by explicitly modelling the underlying multidimensional physics.

Since the early 1990s, when RD techniques were formalised (Struijs 1994, Mesaros 1995, Paillère 1995, Sidilkover and Roe 1995), the literature has shown that RD methods are more accurate than FV methods when applied to the solution of problems on the same size mesh (Paillère 1995, Wood and Kleb 1999, Rad 2001, Wood 2001, Wood and Kleb 2001). Unfortunately, most of the previous studies were more qualitative in nature, usually providing a visual comparison of a given flow feature. There is little to be found on the quantitative comparative accuracy of RD and FV methods, especially with respect to the more practical non-linear distribution methods which are both second-order and monotone. The results of Abgrall (2001) provide some insight, but the quantitative comparisons therein are only in tabular format.

The focus of this research is to compare the accuracy of RD schemes to that of more conventional FV methods. This is achieved by analysing solutions to hyperbolic system of conservation laws having the form

$$\frac{\partial \mathbf{U}}{\partial t} + \vec{\nabla}\cdot\vec{\mathbf{F}} = 0, \tag{1}$$

where $\mathbf{U}$ is the solution vector and $\vec{\mathbf{F}}$ is the flux dyad. The scalar advection equation, non-linear Burgers equation and Euler equations of inviscid compressible gas dynamics in two-space dimensions are all of this form and will be considered here. The latter are especially interesting, not only because of the relevance to practical work, but because it is in the solution of systems that RD

*Corresponding author. Email: groth@utias.utoronto.ca

ISSN 1061-8562 print/ISSN 1029-0257 online

DOI: 10.1080/10618560701748176
http://www.informaworld.com

methods can become more complex. For each case, the spatial order of accuracy will be assessed by determining the dependence of the L_1-error norm of a known quantity as a function of the mesh size.

RD methods were primarily designed for use on unstructured meshes and they tend to perform relatively well even on highly distorted meshes (Paillère 1995, Deconinck *et al.* 2000). This study uses structured quadrilateral meshes, but it is shown in the results that RD methods can also benefit from the structure by optimally tessellating the mesh. Although this research focuses exclusively on the benefits to accuracy, there are several other advantages to the RD method as compared to the FV method. These include (Deconinck *et al.* 2000):

- a multidimensional positivity property; and
- a compact stencil (second-order accuracy can be achieved on a stencil of only one element).

The latter point allows for easier parallelisation of the schemes.

2. Godunov-type FV schemes

Godunov-type FV schemes perform an integration of the solution flux at the boundaries of a cell to compute the cell residual when advancing the solution in time using a time-marching method (Godunov 1959). The solution is often stored and updated at the cell centres. Before computing the flux, the solution in the cell is *reconstructed*, possibly using neighbour cells. A piece-wise constant reconstruction leads to a first-order scheme while a piece-wise linear reconstruction leads to a second-order scheme. To maintain monotonicity, second-order schemes limit the reconstruction, reducing it towards a piece-wise constant when there are large changes in the local solution gradient. The solution fluxes at the cell interfaces are evaluated in terms of the possibly discontinuous reconstructed solution values by solving a Riemann problem. In this study, a Godunov-type FV method developed for body-fitted multiblock mesh is used as the basis for all of the comparisons to the RD schemes. The method incorporates a least-squares piece-wise linear reconstruction, the slope limiter of Venkatakrishnan (1993), and the exact Riemann solver flux function of Gottlieb and Groth (1988). Refer to the paper by Sachdev *et al.* (2005) for a complete description of the FV method.

3. RD for scalar advection

RD methods calculate the residual (or fluctuation) on a element, E, of an unstructured mesh and then, by some appropriate method, distribute the fluctuation to the nodes of that element to advance the solution in time. RD methods are cell-vertex methods that are usually solved on simplexes (triangles in two-space dimensions).

For the scalar advection equation, one has

$$\frac{\partial u}{\partial t} + \sum_{j=1}^{d} \left(\lambda_j \frac{\partial u}{\partial x_j} \right) = 0, \tag{2}$$

where d is the number of dimensions and λ_j is the advection speed in the jth coordinate direction. The fluctuation on a simplex element, E, is defined as

$$\begin{aligned} \phi^E &= -\int_E \frac{\partial u}{\partial t} \mathrm{d}\Omega_E = \int_E \sum_{j=1}^{d} \left(\lambda_j \frac{\partial u}{\partial x_j} \right) \mathrm{d}\Omega_E \\ &= \left[\sum_{j=1}^{d} (\bar{\lambda}_j \hat{x}_j) \right] \cdot \int_E \vec{\nabla} u \, \mathrm{d}\Omega_E, \end{aligned} \tag{3}$$

where Ω_E is the element area, $\hat{x}_j$ defines a unit vector in the jth coordinate direction, and $\bar{\lambda}_j$ is linearised over the element. For non-linear equations, $\bar{\lambda}_j$ is determined via a conservative linearisation such that

$$\left[\sum_{j=1}^{d} (\bar{\lambda}_j \hat{x}_j) \right] \cdot \int_E \vec{\nabla} u \, \mathrm{d}\Omega_E = -\oint_{\partial E} \vec{F}(u) \cdot \hat{n} \, \mathrm{d}\mathcal{S}, \tag{4}$$

where $\hat{n}$ is the inwards-pointing unit normal vector of surface element $\mathrm{d}\mathcal{S}$. For second-order schemes, the solution, u, is assumed to vary linearly in the element. The integral in Equation (3) can then be evaluated exactly to obtain

$$\phi^E = \left[\sum_{j=1}^{d} (\bar{\lambda}_j \hat{x}_j) \right] \cdot \frac{1}{d} \sum_{i=1, i \in E}^{d+1} u_i \vec{n}_i = \sum_{i=1, i \in E}^{d+1} k_i u_i. \tag{5}$$

The index i loops over each node of an element and the vector $\vec{n}_i$ defines the inwards normal of the edge opposite node i and scaled by the length of the edge. The *inflow parameters*, k_i, are defined by

$$k_i = \frac{1}{d} \left[\sum_{j=1}^{d} (\bar{\lambda}_j \hat{x}_j) \right] \cdot \vec{n}_i, \tag{6}$$

and describe whether edge i sees the inflow (positive) or outflow (negative) of the solution quantity. Because $\bar{\lambda}_j$ is linearised, $\sum_{i=1, i \in E}^{d+1} k_i = 0$.

The distribution of the fluctuation to the nodes, ϕ_i^E, is governed by distribution coefficients, β_i, with $\phi_i^E = \beta_i \phi^E$ and where, for consistency, $\sum_{i, i \in E}^{d+1} \beta_i = 1$. The nodal residual is defined as the sum of all fluctuations distributed to node i from all elements, E, that share node i as a vertex. The semi-discrete update

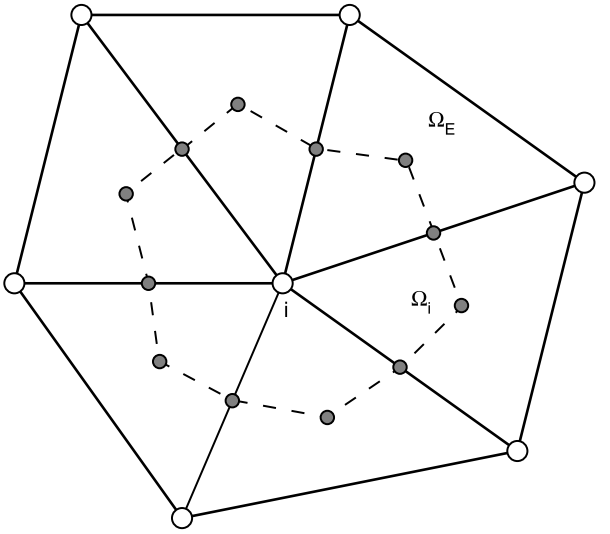

Figure 1. Primary elements (solid lines) and dual mesh (dashed lines) created from element centroids and edge midpoints.

formula is then

$$\Omega_i \frac{\mathrm{d}u_i}{\mathrm{d}t} + \sum_E \beta_i^E \phi^E = 0, \tag{7}$$

where Ω_i is the area of the dual mesh, shown in Figure 1, associated with node i of the unstructured mesh. Various time-marching schemes can be applied to the solution of the ordinary differential equations for the nodal values of the solution.

In two dimensions, one can envision two possible orientations of the elemental triangles: those with one downstream vertex (one positive inflow parameter – type I triangle in Figure 2) and those with two downstream vertices (two positive inflow parameters – type II triangle in Figure 2). In the former case, all the fluctuation is sent to the downstream vertex. In the latter case, the fluctuation is split between the two downstream nodes.

Characteristics of the various RD schemes are defined by the distribution coefficients, β_i. Some common schemes and their key properties are listed in Table 1. Schemes that are positive (P) are monotonic while those that are linearity-preserving (LP) achieve higher orders of accuracy (second-order for a linear interpolation of the fluctuation). It is sufficient that the distribution coefficients are bounded for a scheme to be LP (Deconinck *et al.* 2000). In this study, LDA, LN and blended B (non-linear combinations of N and LDA) distributions schemes are considered.

Table 1. Distinguishing properties of RD schemes.

Scheme	Linearity	P	LP
N	Linear	√	–
LDA	Linear	–	√
LN	Non-linear	√	√
B	Non-linear	√[a]	√

[a] Positivity has not been formally demonstrated but is usually assumed based on numerical results.

The *N* scheme is formulated by ensuring that positivity is preserved (Deconinck *et al.* 1991, Paillère 1995):

$$\phi_i^N = k_i^+ (u_i - u_{\mathrm{in}}), \tag{8}$$

where

$$u_{\mathrm{in}} = \frac{\sum_{j=1, j\in E}^{d+1} k_j^- u_j}{\sum_{j=1, j\in E}^{d+1} k_j^-}. \tag{9}$$

The distribution coefficients for the *N* scheme are not bounded and may tend to $\pm\infty$ as $\phi^E \to 0$. For the LDA scheme, the distribution is governed by the location at which the linearised characteristic vector intersects the outflow edge. In Figure 3, $\beta_i = L_i/L$ and $\beta_j = L_j/L$. This is more conveniently expressed as

$$\beta_i^{\mathrm{LDA}} = -\frac{k_i^+}{\sum_{j=1, j\in E}^{d+1} k_j^-}. \tag{10}$$

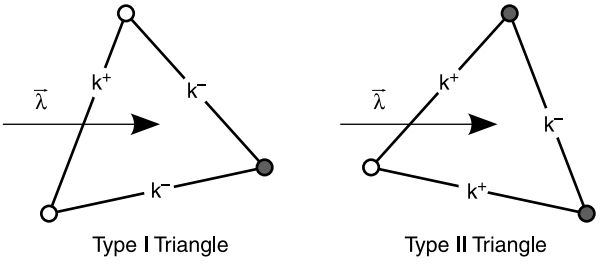

Figure 2. Possible triangle orientations in a two-dimensional flow. $\bar{\lambda}$ is the linearised characteristic vector.

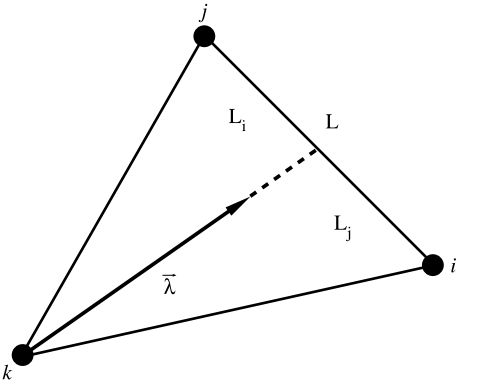

Figure 3. The LDA distribution is governed by the location $\bar{\lambda}$ intersects the outflow edge.

The LN scheme is based upon the N scheme but limits the distribution coefficients when one of them (in the case of a type II triangle) becomes negative. If ϕ_1^N and ϕ_2^N denote the fluctuation that would be distributed to the two downstream nodes by the N scheme and $r = -\phi_1^N/\phi_2^N$, then the limited distribution given by the LN scheme is

$$\phi_1^{\mathrm{LN}} = \phi_1^N\left[1 - \frac{\psi(r)}{r}\right], \quad \phi_2^{\mathrm{LN}} = \phi_2^N[1 - \psi(r)], \tag{11}$$

where $\psi(r)$ is a symmetric limiter. Use of a minmod limiter,

$$\psi(r) = \max[0, \min(r, 1)], \tag{12}$$

produces a scheme identical to the positive-streamwise-invariant (PSI) scheme of Struijs (1994) that is often quoted in the literature. This equivalence was originally reported by Sidilkover and Roe (1995).

The blended scheme is a blending of the N and LDA schemes, $\phi^B = \theta\phi^N + (1 - \theta)\phi^{\mathrm{LDA}}$. There are several possible definitions of the blending coefficient θ; see (Abgrall 2001) for a definition that reproduces the PSI scheme. In this work, the heuristic definition proposed by Deconinck *et al.* (2000),

$$\theta = \frac{|\phi^E|}{\sum_{l=1,l\in E}^{d+1}|\phi_l^N| + \epsilon}, \quad \epsilon = 10^{-10}, \tag{13}$$

is used where θ is defined to switch to the LDA scheme when divergence of the nodal fluctuation, as computed by the N-scheme, is detected. Positivity of this particular blended scheme has not been formally shown; however, numerical experiments generally produce solutions that are satisfactorily monotone.

Although representative of *base* schemes, the list in Table 1 is not exhaustive nor illustrative of the most recent or advanced techniques. In particular, a reader interested in non-linear schemes may want to review 'mapped' distribution schemes (Abgrall and Roe 2003, Abgrall and Mezine 2004, Abgrall 2006). These schemes are of interest because they are extensible to any number of dimensions; nevertheless, in two dimensions, the objective is still to reproduce the PSI scheme.

4. RD for the Euler equations

The two-dimensional Euler equations are given by Equation (1) with

$$\mathbf{U} = \begin{bmatrix} \rho \\ \rho u \\ \rho v \\ \rho e_{\mathrm{T}} \end{bmatrix}, \quad \mathbf{F}_x = \begin{bmatrix} \rho u \\ \rho u^2 + p \\ \rho uv \\ \rho u h_{\mathrm{T}} \end{bmatrix}, \quad \mathbf{F}_y = \begin{bmatrix} \rho v \\ \rho uv \\ \rho v^2 + p \\ \rho v h_{\mathrm{T}} \end{bmatrix}, \tag{14}$$

where e_{T} is the specific total energy and h_{T} is the specific total enthalpy. In this work, gaseous flows of air are considered and the preceding partial differential equations are supplemented with the ideal gas law, $p = \rho RT$, as an equation of state. The specific gas constant, R, is taken to be 287 J/kg K and a perfect gas is assumed with a specific heat ratio of $\gamma = 1.4$. In quasi-linear form, Equation (1) with (14) becomes

$$\frac{\partial \mathbf{U}}{\partial t} + \sum_{j=1}^{d}\left(\mathbf{A}_{U,j}\frac{\partial \mathbf{U}}{\partial x_j}\right) = 0, \tag{15}$$

where $\mathbf{A}_{U,j} = \partial\mathbf{F}_j/\partial\mathbf{U}$ are the conservative-variable flux Jacobians.

For systems of equations, the scalar inflow parameters, k_i, of the RD schemes become matrices, $\mathbf{K}_i$, since the linearised scalar wave speed, $\bar{\lambda}_j$, of Equation (4) is now a matrix that depends on the linearised flux Jacobians

$$\bar{\mathbf{A}}_{U,j} = \frac{\partial \mathbf{F}_j}{\partial \mathbf{U}}\Big|_{\bar{\mathbf{S}}}. \tag{16}$$

The notation of Equation (16) denotes that the Jacobian is linearised at the average state $\bar{\mathbf{S}} = (1/(d+1))\sum_{i,i\in E}^{d+1}\mathbf{S}_i$ of a set of, as yet undefined, solution variables $\mathbf{S}(\mathbf{U})$. Equation (6) then has the form

$$\mathbf{K}_i = \frac{1}{d}\left[\sum_{j=1}^{d}(\bar{\mathbf{A}}_j\hat{x}_j)\right]\cdot\vec{n}_i. \tag{17}$$

Having matrices as inflow parameters creates two primary issues. The first is to find a method of linearisation, i.e. a definition of $\mathbf{S}_i$, that is still conservative. The second is the technique for computing the distribution coefficients, β_i, which are now matrices.

4.1 Linearisation

A conservative linearisation has been found for the Euler equations. The Roe–Struijs–Deconinck linearisation (Struijs 1994) is an extension of Roe's parameter vector to multiple dimensions $\mathbf{S} = \mathbf{Z} = [\sqrt{\rho}, \sqrt{\rho}u, \sqrt{\rho}v, \sqrt{\rho}h]^{\mathrm{T}}$. This linearisation ensures that a conservative fluctuation may be computed as

$$\phi_U^E = \sum_{i=1, i\in E}^{d+1} \mathbf{K}_{U,i}\tilde{\mathbf{U}}_i, \tag{18}$$

where $\tilde{\mathbf{U}}_i = (\partial\mathbf{U}/\partial\mathbf{S})|_{\tilde{\mathbf{S}}}\mathbf{S}_i$. Use of a conservative linearisation leads to a linearisation-based RD (LRD) scheme. Unfortunately, conservative linearisations are not available for all systems of equations. Also, in some cases the use of $\mathbf{Z}$ as the linearised state may be undesirable. In particular, non-existent pressure gradients may be detected for shear flows (Mesaros 1995).

An alternative to using a conservative linearisation is to use a contour-integration-based RD (CRD) scheme (Csík *et al.* 2002). In this technique, the fluctuation is computed via a contour integral given by

$$\phi^E = -\oint_{\partial E} \vec{\mathbf{F}}(\mathbf{S})\cdot\hat{n}\,\mathrm{d}\mathcal{S}, \tag{19}$$

where, in a numerical implementation, a Gauss quadrature integration rule is used to evaluate the integral. In the subsequent distribution step, any set of variables $\mathbf{S}$ may be used for the linearisation. Since it is no longer true that $\phi_U^E = \sum_{i=1,i\in E}^{d+1}\mathbf{K}_{U,i}\tilde{\mathbf{U}}_i$, the N scheme must be modified to ensure conservation. For scalar equations, Equation (9) is replaced by

$$u_{\mathrm{in}} = -\frac{\sum_{i=1,i\in E}^{d+1} k_i^+ u_i - \phi^E}{\sum_{i=1,i\in E}^{d+1} k_i^-}. \tag{20}$$

Note that if a conservative linearisation is still used, this modification does not change anything because $\sum_{i=1,i\in E}^{d+1} k_i^- u_i = \phi^E - \sum_{i=1,i\in E}^{d+1} k_i^+ u_i$. Also, no modifications are required for the LDA scheme since $\sum_{i=1,i\in E}^{d+1}\beta_i^{\mathrm{LDA}} = 1$, irrespective of the linearisation, and therefore the distributed fluctuation is conserved. Although the CRD technique is rather simple, the effects are profound because RD solutions are no longer restricted to a particular linearisation. The Euler results in this study are all obtained using a CRD scheme with a linearisation based on the primitive variables $\mathbf{S} = \mathbf{V} = [\rho, u, v, p]^{\mathrm{T}}$.

4.2 System distribution

There are currently two approaches to distributing the fluctuation for a system: system decomposition and matrix schemes (Deconinck *et al.* 2000). The most physically satisfactory approach is to decompose the system into scalar equations. This is achieved via hyperbolic–elliptic splitting where, for the steady Euler equations, the addition of a preconditioner allows for diagonalisation of the equations in characteristic form (Mesaros 1995, Paillère 1995, Rad 2001). Matrix schemes are a generalisation of scalar techniques to matrix-vector equations. Although not as intuitive nor physically meaningful as equation decomposition techniques, the resulting schemes can still provide very accurate results.

4.2.1 System decomposition

Hyperbolic–elliptic splitting provides a method for decomposing the Euler equations. Supersonic flows decouple into four scalar equations while subsonic flows decouple into two scalar equations plus an acoustic subset. In this work, only the details describing the implementation are described. Details regarding the development of the related preconditioner are available elsewhere (Mesaros 1995, Paillère 1995, Rad 2001).

For simplicity, the Euler equations are expressed in terms of a particular set of symmetrising variables, $\breve{\mathbf{Q}}$, as follows

$$\frac{\partial\breve{\mathbf{Q}}}{\partial t} + \mathbf{A}_{\breve{Q}}\frac{\partial\breve{\mathbf{Q}}}{\partial x} + \mathbf{B}_{\breve{Q}}\frac{\partial\breve{\mathbf{Q}}}{\partial y} = 0, \tag{21}$$

before applying the preconditioner. The symmetrising variables have the form

$$\partial\breve{\mathbf{Q}} = [\partial p/(\rho a), \partial q,\ q\partial\theta,\ \partial S]^{\mathrm{T}}, \tag{22}$$

where q is the flow speed

$$q = \sqrt{u^2 + v^2}, \quad \partial q = \frac{u\partial u + v\partial v}{q}, \tag{23}$$

θ is the local flow direction

$$\theta = \tan^{-1}\frac{v}{u}, \quad \partial\theta = \frac{u\partial v - v\partial u}{q^2}, \tag{24}$$

and ∂S is proportional to the change in entropy

$$\partial S = \partial p - a^2\partial\rho. \tag{25}$$

The preconditioner, $\mathbf{P}$, is added such that

$$\frac{\partial\breve{\mathbf{Q}}}{\partial t} + \mathbf{P}\left(\mathbf{A}_{\breve{\mathbf{Q}}}\frac{\partial\breve{\mathbf{Q}}}{\partial x} + \mathbf{B}_{\breve{Q}}\frac{\partial\breve{\mathbf{Q}}}{\partial y}\right) = 0. \tag{26}$$

Note that the preconditioning does not affect steady-state solutions. This system may be re-written as

$$\mathbf{A}_{\breve{Q}}^{-1}\mathbf{P}^{-1}\frac{\partial\breve{\mathbf{Q}}}{\partial t}+\frac{\partial\breve{Q}}{\partial x}+\mathbf{A}_{\breve{Q}}^{-1}\mathbf{B}_{\breve{Q}}\frac{\partial\breve{Q}}{\partial y}=0. \tag{27}$$

The matrix $\mathbf{A}_{\breve{Q}}^{-1}\mathbf{B}_{\breve{Q}}$ can be diagonalised as $\mathbf{\Lambda}=\mathbf{L}\mathbf{A}_{\breve{Q}}^{-1}\mathbf{B}_{\breve{Q}}\mathbf{R}$ and thereby defining the characteristic variables $\partial\mathbf{W}=\mathbf{L}\partial\mathbf{Q}$. After diagonalisation and a change of variables from $\mathbf{Q}$ to $\mathbf{W}$, Equation (27) assumes the form

$$\mathbf{L}\mathbf{A}_{\breve{Q}}^{-1}\mathbf{P}^{-1}\mathbf{R}\frac{\partial\mathbf{W}}{\partial t}+\frac{\partial\mathbf{W}}{\partial x}+\mathbf{\Lambda}\frac{\partial\mathbf{W}}{\partial y}=0. \tag{28}$$

The preconditioner is defined to diagonalise the matrix $\mathbf{D}=\mathbf{L}\mathbf{A}_{\breve{Q}}^{-1}\mathbf{P}^{-1}\mathbf{R}$, completely for supersonic flows and as much as possible for subsonic flows. A preconditioner, valid for both subsonic and supersonic flows, can be written as

$$\mathbf{P}=\begin{bmatrix}\frac{\alpha\chi M^2}{\beta} & -\frac{\alpha\chi M}{\beta} & 0 & 0\\ -\frac{\alpha\chi M}{\beta} & \frac{\alpha\chi}{\beta}+\alpha & 0 & 0\\ 0 & 0 & \beta\chi & 0\\ 0 & 0 & 0 & \alpha\end{bmatrix}, \tag{29}$$

where $\beta=\sqrt{\max(\epsilon^2,|M^2-1|)}$ and $\chi=1/\max(M,1)$. To avoid problems at the sonic point, ϵ assumes a small value, typically 0.05 (Paillère 1995). The quantity α was introduced by Mesaros (1995) to reduce sensitivity to the flow angle in stagnation regions. It is defined as

$$\alpha=\begin{cases}\frac{1}{2}, & \text{for } M\le\frac{1}{3},\\ \frac{1}{2}+\frac{27}{2}\left(M-\frac{1}{3}\right)^2-27\left(M-\frac{1}{3}\right)^3, & \text{for } \frac{1}{3}<M<\frac{2}{3},\\ 1, & \text{for } M\ge\frac{2}{3}\end{cases}$$

Equation (28) then takes the form

$$\frac{\partial\mathbf{W}}{\partial t}+\mathbf{A}_W\frac{\partial\mathbf{W}}{\partial x}+\mathbf{B}_W\frac{\partial\mathbf{W}}{\partial y}=0, \tag{30}$$

where $\mathbf{A}_W=\mathbf{D}^{-1}$ and $\mathbf{B}_W=\mathbf{D}^{-1}\mathbf{\Lambda}$. The characteristic variables are given by

$$\partial\mathbf{W}=\begin{bmatrix}\partial S\\ \frac{1}{\rho q}\partial p+\partial q\\ \frac{\beta}{\rho q}\partial p+q\partial\theta\\ \frac{\beta}{\rho q}\partial p-q\partial\theta\end{bmatrix}. \tag{31}$$

A prescription of $\mathbf{A}_W$ and $\mathbf{B}_W$ that is valid for both supersonic and subsonic flows and encompasses a smooth transition between the two regimes is given by

$$\mathbf{A}_W=\begin{bmatrix}\alpha u & 0 & 0 & 0\\ 0 & \alpha u & 0 & 0\\ 0 & 0 & \frac{1}{2}\chi[u\beta(\alpha\eta+1)-v(\alpha+1)] & \frac{1}{2}\chi[u\beta(\alpha\eta-1)+v(\alpha-1)]\\ 0 & 0 & \frac{1}{2}\chi[u\beta(\alpha\eta-1)-v(\alpha-1)] & \frac{1}{2}\chi[u\beta(\alpha\eta+1)+v(\alpha+1)]\end{bmatrix}, \tag{32}$$

$$\mathbf{B}_W=\begin{bmatrix}\alpha v & 0 & 0 & 0\\ 0 & \alpha v & 0 & 0\\ 0 & 0 & \frac{1}{2}\chi[v\beta(\alpha\eta+1)+u(\alpha+1)] & \frac{1}{2}\chi[v\beta(\alpha\eta-1)-u(\alpha-1)]\\ 0 & 0 & \frac{1}{2}\chi[v\beta(\alpha\eta-1)+u(\alpha-1)] & \frac{1}{2}\chi[v\beta(\alpha\eta+1)-u(\alpha+1)]\end{bmatrix}, \tag{33}$$

where $\eta=(M^2-1)/\beta^2$. Note that η is defined as -1 for subsonic flows and $+1$ for supersonic flow but it smoothly transitions between the two values over the range $1-\epsilon^2<M^2<1+\epsilon^2$. In supersonic flows, matrices (32) and (33) are diagonal and have the form

$$\mathbf{A}_w=\begin{bmatrix}u & 0 & 0 & 0\\ 0 & u & 0 & 0\\ 0 & 0 & \frac{u\beta-v}{M} & 0\\ 0 & 0 & 0 & \frac{u\beta+v}{M}\end{bmatrix}, \tag{34}$$

$$\mathbf{B}_w = \begin{bmatrix} v & 0 & 0 & 0 \\ 0 & v & 0 & 0 \\ 0 & 0 & \frac{v\beta+u}{M} & 0 \\ 0 & 0 & 0 & \frac{v\beta-u}{M} \end{bmatrix}.$$

The following steps summarise the numerical implementation of the RD scheme resulting from the hyperbolic–elliptic equation decomposition procedure:

(1) The fluctuation in conservative variables, ϕ_U^E, is computed using Equation (19).
(2) The average linearised state is determined and used to compute the transformation matrices $\partial\breve{\mathbf{Q}}/\partial\mathbf{U}$, $\partial\mathbf{U}/\partial\breve{\mathbf{Q}}$, $\partial\mathbf{W}/\partial\breve{\mathbf{Q}}$, $\partial\breve{\mathbf{Q}}/\partial\mathbf{W}$ and $\partial\mathbf{U}/\partial\mathbf{V}$ as well as the preconditioner $\mathbf{P}$.
(3) The fluctuation is preconditioned and transformed into characteristic variables via

$$\phi_W^E = \frac{\partial\mathbf{W}}{\partial\breve{\mathbf{Q}}}\mathbf{P}\frac{\partial\breve{\mathbf{Q}}}{\partial\mathbf{U}}\phi_U^E.$$

(4) The solution state at each vertex in the element is converted from the linear state (primitive variables in this work) to characteristic variables via

$$\tilde{\mathbf{W}}_i = \frac{\partial\mathbf{W}}{\partial\breve{\mathbf{Q}}}\frac{\partial\breve{\mathbf{Q}}}{\partial\mathbf{U}}\frac{\partial\mathbf{U}}{\partial\mathbf{V}}\mathbf{V}_i.$$

(5) The fluctuation is distributed using scalar distribution everywhere except for the elliptic subset which arises from the acoustic equations in a subsonic flow. In this work, the elliptic subset is distributed using a Lax–Wendroff scheme (Mesaros 1995),

$$\beta_i^{\mathrm{LW}} = \frac{\hat{\mathbf{I}}}{3} + \frac{\tau}{2\Omega_E}\mathbf{K}_{W,i}, \tag{35}$$

where $\hat{\mathbf{I}}$ is the identity matrix and τ/Ω_E is set to the maximum eigenvalue of matrix $\mathbf{K}_{W,i}$. The acoustic inflow parameter $\mathbf{K}_{W,i}$ is formulated using Equation (17) but only using the 2×2 acoustic subsets of $\mathbf{A}_W$ and $\mathbf{B}_W$. Note that more sophisticated elliptic distribution techniques exist, but are not considered as part of this work. The most advanced is probably the least-squares minimisation technique advocated by Rad (2001).
(6) The fluctuation at each vertex is converted to conservative variables for the update of the solution. At this point, there is the option to retain or remove the preconditioner (Mesaros 1995, Paillère 1995). The most consistent method is to remove the preconditioner from the distributed element fluctuation and reapply it, if desired for convergence acceleration, at the vertex. This conversion is performed as follows:

$$\phi_{U,i} = \frac{\partial\mathbf{U}}{\partial\breve{\mathbf{Q}}}\mathbf{P}^{-1}\frac{\partial\breve{\mathbf{Q}}}{\partial\mathbf{W}}\phi_{W,i}.$$

This method is fully conservative but less computationally robust. The preconditioner may alternatively be retained in the fluctuation by the following conversion

$$\phi_{U,i} = \frac{\partial\mathbf{U}}{\partial\breve{\mathbf{Q}}}\frac{\partial\breve{\mathbf{Q}}}{\partial\mathbf{W}}\phi_{W,i}.$$

This implies an assumption that the preconditioners in each of the elements sharing vertex i are sufficiently close in value. In other words, the flow is smooth. This approach is not conservative but numerical experiments indicate that it is more robust (about the same as a matrix RD scheme). The two approaches yield similar results, even in the vicinity of strong discontinuities, but the conservative method was found to be more accurate. In this work, the conservative approach is used for all the decomposed solutions.
(7) The desired time-marching algorithm is applied to the discrete solution at each vertex governed by the semi-discrete form of the governing equations given by Equation (7). For explicit time-marching, the preconditioner, computed at the vertex state, is typically reapplied to the vertex residual if it was removed in the previous step. Otherwise, extremely small time-steps are required.

A troublesome problem inherent to hyperbolic–elliptic splitting is that the preconditioned system suffers from a degeneracy in the system eigenvectors and a sensitivity to the flow angle in the stagnation limit. While Mesaros (1995) has reduced the sensitivity to the flow angle as described above (Equation (29)), there is currently no systematic fix for resolving the degeneracy. Because of this issue, system decomposition is not applied herein for flow problems with stagnation points.

4.2.2 *Matrix distribution*

Matrix distribution schemes are generalisations of scalar techniques (van der Weide *et al.* 1999). The particular class of schemes considered here are all invariant under a similarity transformation, meaning that the same conservative fluctuation is sent to the vertices, irrespective of the variables in which the distribution is actually performed (Deconinck *et al.* 2000). It is therefore

beneficial to switch to the symmetrising variables

$$\partial \mathbf{Q} = [\partial p/(\rho a),\ \partial u,\ \partial v,\ \partial S]^{\mathrm{T}}, \tag{36}$$

where $\partial S = \partial p - a^2 \partial \rho$, when formulating the distribution scheme. The matrices $\mathbf{A}_Q$ and $\mathbf{B}_Q$ assume the form

$$\mathbf{A}_Q = \begin{bmatrix} u & a & 0 & 0 \\ a & u & 0 & 0 \\ 0 & 0 & u & 0 \\ 0 & 0 & 0 & u \end{bmatrix}, \quad \mathbf{B}_Q = \begin{bmatrix} v & 0 & a & 0 \\ 0 & v & 0 & 0 \\ a & 0 & v & 0 \\ 0 & 0 & 0 & v \end{bmatrix}. \tag{37}$$

In symmetrising form, the last equation completely decouples from the system. This is the entropy advection equation. As a result, only the upper 3×3 subset remains to be solved by matrix distribution. In what follows, the inflow parameters $\mathbf{K}_Q$ are formulated using Equation (17) but only for the upper 3×3 subset of $\mathbf{A}_Q$ and $\mathbf{B}_Q$.

Matrix versions of the N, LDA and blended distribution schemes are now described. For all the schemes, the inflow parameters $\mathbf{K}_Q$ must first be split into positive and negative components. Matrix $\mathbf{K}_Q$ is diagonalised via $\mathbf{\Lambda} = \mathbf{L}\mathbf{K}_Q\mathbf{R}$. Using $\mathbf{\Lambda}^{\pm} = (\mathbf{\Lambda} \pm |\mathbf{\Lambda}|)/2$, the split inflow parameters are defined as $\mathbf{K}_Q^{\pm} = \mathbf{R}\mathbf{\Lambda}^{\pm}\mathbf{L}$. The matrix N scheme then defines the fluctuation distributed to each node i of an element as

$$\phi_{Q,i}^N = \mathbf{K}_{Q,i}^+(\tilde{\mathbf{Q}}_i - \mathbf{Q}_{\mathrm{in}}). \tag{38}$$

The modified state $\mathbf{Q}_{\mathrm{in}}$ for the CRD scheme is

$$\mathbf{Q}_{\mathrm{in}} = -\mathbf{N}\left(\sum_{j=1,j\in E}^{d+1} \mathbf{K}_{Q,j}^+ \tilde{\mathbf{Q}}_j - \phi_Q^E\right), \tag{39}$$

where

$$\mathbf{N} = \left(\sum_{j=1,j\in E}^{d+1} \mathbf{K}_{Q,j}^-\right)^{-1}. \tag{40}$$

For the matrix LDA scheme, $\phi_{Q,i}^{\mathrm{LDA}} = \beta_i^{\mathrm{LDA}}\phi_Q^E$ where

$$\beta_i^{\mathrm{LDA}} = -\mathbf{K}_{Q,i}^+\mathbf{N}. \tag{41}$$

At stagnation points, the matrix $\mathbf{N}$ may become singular. Analytically, it has been shown that $\mathbf{K}_{Q,i}^+\mathbf{N}$ always has meaning (Abgrall 2001). Numerically, a small modification to $\mathbf{K}_{Q,i}^{\pm}$ is made when

$$\sum_{j=1,j\in E}^{d+1} \bar{\vec{q}}\cdot\vec{n}_j < 1 \times 10^{-3}\mathrm{m/s}, \tag{42}$$

($\bar{\vec{q}}$ is the linearised velocity in the element). At stagnation points, $\sum_{j=1,j\in E}^{d+1}\mathbf{K}_{Q,j}^-$ assumes the form

$$\begin{bmatrix} s_{11} & 0 & 0 \\ 0 & s_{22} & s_{23} \\ 0 & s_{23} & s_{33} \end{bmatrix}.$$

This matrix is singular when $s_{22}s_{33} - s_{23}^2 = 0$, something that is also true at stagnation points. When a stagnation region is encountered (Equation (42) is true) a simple modification to avoid the singularity is introduced:

$$K_{Q,i,22}^+ = K_{Q,i,22}^+ + \epsilon \quad K_{Q,i,33}^+ = K_{Q,i,33}^+ + \epsilon$$

$$K_{Q,i,22}^- = K_{Q,i,22}^- - \epsilon \quad K_{Q,i,33}^- = K_{Q,i,33}^- - \epsilon,$$

where ϵ assumes a small value, typically 1×10^{-6}. Note that this procedure has no effect on the overall value of $\mathbf{K}_{Q,i}$.

For systems, use of the LN scheme is not straightforward so non-linear distributions are commonly obtained by applying blends of the N and LDA schemes. The fluctuation distributed by the blended B scheme is

$$\phi_{Q,i}^B = \mathbf{\Theta}\phi_{Q,i}^N + (\hat{\mathbf{I}} - \mathbf{\Theta})\phi_{Q,i}^{\mathrm{LDA}}, \tag{43}$$

where $\hat{\mathbf{I}}$ is the identity matrix. The entries of the diagonal non-linear blending matrix $\mathbf{\Theta}$ are given by

$$\mathbf{\Theta}_{k,k} = \frac{|\phi_{Q,k}^E|}{\sum_{l=1,l\in E}^{d+1}|\phi_{Q,l,k}^N| + \epsilon}, \quad \epsilon = 10^{-10}, \tag{44}$$

where index k refers the kth equation of the system and l loops over the vertices of the element (Deconinck *et al.* 2000, Csík *et al.* 2002).

The following steps summarise the numerical implementation of the RD scheme resulting from the matrix distribution procedure applied to the Euler equations:

(1) The fluctuation in conservative variables, ϕ_U^E, is computed using Equation (19).
(2) The average linearised state is determined and used to compute the transformation matrices $\partial\mathbf{Q}/\partial\mathbf{U}$, $\partial\mathbf{U}/\partial\mathbf{Q}$ and $\partial\mathbf{U}/\partial\mathbf{V}$.
(3) The fluctuation is transformed into symmetrising variables via

$$\phi_Q^E = \frac{\partial\mathbf{Q}}{\partial\mathbf{U}}\phi_U^E.$$

(4) The solution state at each vertex in the element is converted from the linear state (primitive variables in this work) to symmetrising variables via

$$\tilde{\mathbf{Q}}_i = \frac{\partial \mathbf{Q}}{\partial \mathbf{U}} \frac{\partial \mathbf{U}}{\partial \mathbf{V}} \mathbf{V}_i.$$

(5) The entropy equation is distributed using a scalar method and the remaining 3×3 subset by a matrix technique.

(6) The fluctuation at each vertex is converted to conservative variables for the update

$$\phi_{U,i} = \frac{\partial \mathbf{U}}{\partial \mathbf{Q}} \phi_{Q,i}.$$

(7) The desired time-marching algorithm is applied at each vertex using the semi-discrete update formula of Equation (7).

5. Implementation details

Some other details concerning the present implementation of the RD schemes are now discussed. This includes the method of grid tessellation, boundary conditions (BCs) and the time-marching algorithm.

5.1 Grid tessellation

Standard RD methods are solved on a grid of simplexes (triangles in two dimensions). The approach adopted here for applying the schemes to structured quadrilateral grids is to insert a diagonal into each quadrilateral thereby triangulating the mesh. It is therefore possible to take advantage of the freedom to optimally align the diagonal with the characteristic vector. In Section 6.1, the effects of choosing an optimal direction for the diagonal are examined for scalar equations.

For scalar equations, the optimal diagonal is aligned with the advection vector. For solutions of the Euler equations by matrix distribution or subsonic decomposition, the diagonal is aligned with the streamline vector. The same procedure can be applied when decomposing the Euler equations in supersonic flows, but in some cases this will cause the diagonal to be inserted in a direction that is opposite to the direction of the dominant wave. An example of this is illustrated in Figure 4. In this case, the incident supersonic flow is oriented in a direction from the top left to the bottom right. An oblique shock produced by a solid wall aligned with the x-axis at $y = 0$ turns the flow to the horizontal or x-direction. The streamline in the incident flow (and through a finite shock) is therefore oriented in a direction that is opposite to the direction of the shock wave. The shock is the only significant wave in the flow and ideally the diagonals should be aligned with this wave. Figure 4(a),(b) show the grid and exact solution, respectively. A matrix distribution using a blended scheme with a streamline tessellation is shown in Figure 4(c). A decomposed solution (the flow is entirely supersonic so the Euler equations decouple into four scalar equations) using an LN scheme with a streamline tessellation is shown in Figure 4(d). Both of these are more dissipative than if the tessellation had been fixed in the orientation of the shock prior to the solution. In Figure 4(e), each scalar wave resulting from the decoupled Euler equations is solved on a tessellation aligned with its own characteristic velocity. The shock is much more compact but numerous spurious waves are produced behind the shock. The reasons for these waves are currently not fully understood. In Figure 4(f), both streamline waves are solved on a tessellation aligned with the streamline, and both acoustic waves are solved on a tessellation aligned with the dominant acoustic wave. This technique seems to eliminate the spurious waves and is used for all of the results given in the remainder of the paper.

Note that when a separate tessellation is used for the streamline and acoustic waves, the linear state is averaged over the entire quadrilateral and conservation is maintained on the quadrilateral. Since all transformation matrices are computed at the same state, and since the CRD linearisation technique allows conservation to be independent of the linear state, the scheme is still conservative. The dominant acoustic wave is determined by comparing the difference in the acoustic characteristic variables between opposite vertices in the quadrilateral. The dominant wave is assumed to run counter to the largest difference. Note also that the tessellation is frozen at a prescribed level of convergence so as not to interfere with the convergence of the solution.

5.2 Boundary conditions

BCs are implemented using a weak formulation originally proposed by Paillère (1995). In Figure 5, the BCs for vertex V1 are prescribed indirectly via two ghost elements, GE1 and GE2. The ghost elements are degenerate with the dashed lines having zero length. The ghost vertices, GV1 and GV2, therefore lie directly on top of vertex V1. The states in the ghost vertices are set to produce the desired results, e.g. far-field conditions for a far-field BC and reflected velocity for a symmetry or inviscid wall BC. For the purpose of calculating the time-step, the area of each ghost cell is taken to be half the area of the dual mesh associated with vertex V1.

Paillère (1995) recommends using all three nodes in the ghost cell to set the linearised state. However, in this work the linear state is based only on V1, reasoning that V2 and V3 should not have any influence because of the collapsed edges. Additionally, the state in the ghost

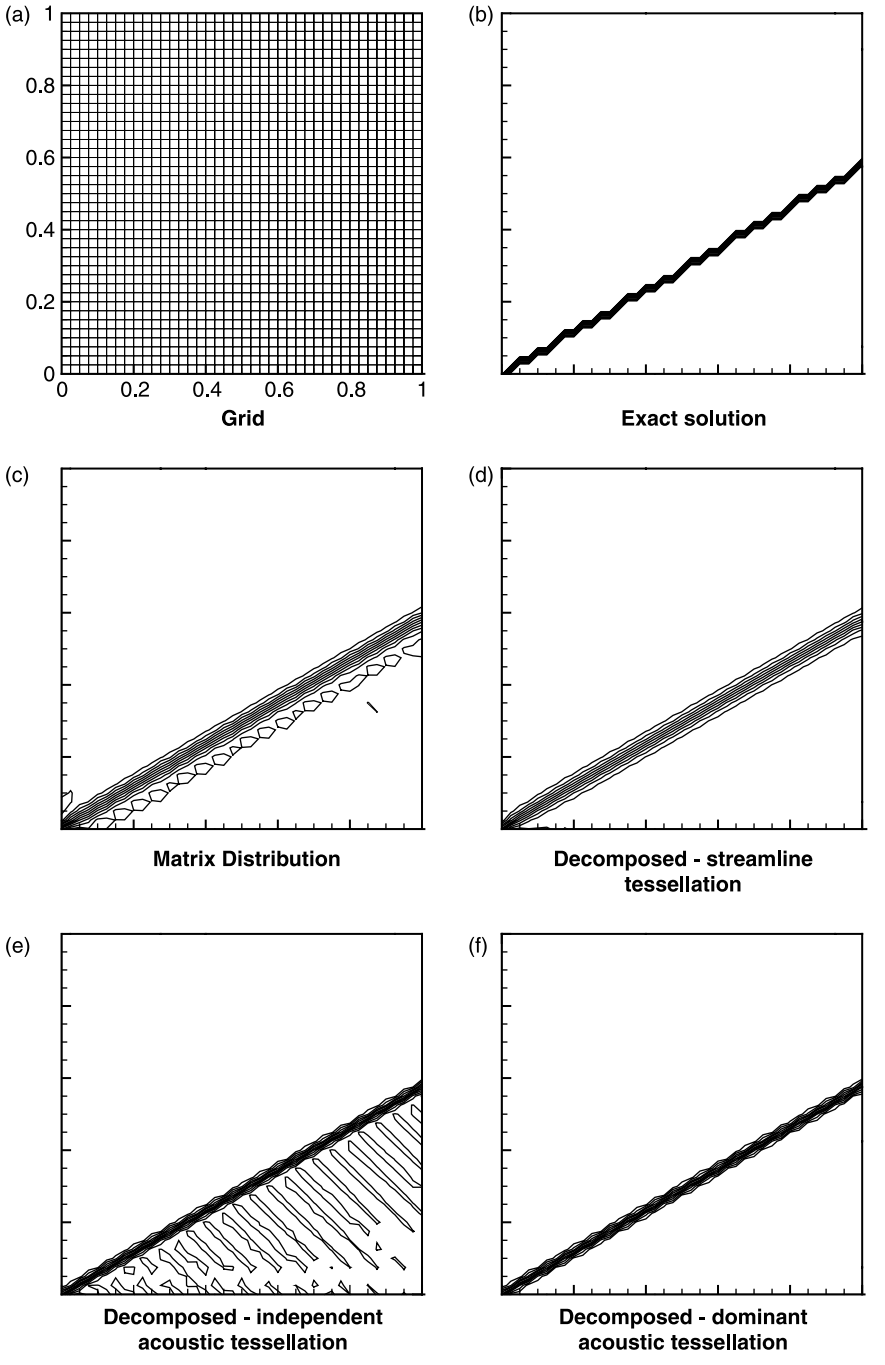

Figure 4. Distribution of pressure for solution of an oblique shock. The effect of various tessellations are examined. The incident flow is at Mach 2 and orientated at -13.8978° to the wall (for a shock inclined at 30° to the wall)

vertices could be irrelevant, e.g. consider a far-field boundary in a region of supersonic outflow. Nevertheless, in some subsonic cases, using all three nodes to calculate the linearised state does seem to produce better results.

5.3 Time-marching algorithm

A simple explicit-Euler time-marching algorithm is used to advance the solution in time. The time step in each element is computed as

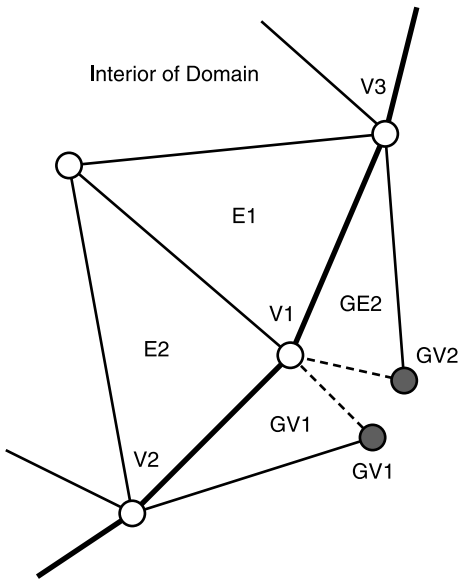

Figure 5. Weak BC consisting of ghost elements, GE1 and GE2, and ghost vertices, GV1 and GV2.

$$h^E = \frac{1}{3}\frac{\Omega^E}{k_{\max}}, \tag{45}$$

a restriction that ensures positivity for a scalar N scheme. For scalar equations, $k_{\max}$ is the maximum inflow parameter in the element. For matrix-distribution techniques, $k_{\max}$ is the maximum eigenvalue over all the $\mathbf{K}_{i,i\in E}$ matrices. For the scalar equations, a Courant–Friedrichs–Lewy (CFL) number of 2 is used. For supersonic Euler solutions, a CFL number of 1.5 is used. In all other flows, a CFL number of unity is used.

6. Numerical results

The numerical accuracies of the RD and FV schemes were compared for solutions of the scalar advection equation, the scalar non-linear Burgers equation and the Euler equations. In each case, the qualitative accuracy is shown by comparing computed distributions of the solutions and the quantitative accuracy is shown by comparing solution errors. Graphs of the solution errors illustrate the variation of the L_1-error norms for a given quantity with respect to the square root of the number of grid points N_D (i.e. the dimensional spacing of the computational grid). The L_1-error norm of the solution error is computed as

$$L_1\text{-error} = \frac{\int |u - u_{\text{exact}}| \mathrm{d}\Omega}{\Omega}, \tag{46}$$

where u_{exact} is the exact solution to the problem as determined by analysis. The variation of the error as a function of N_D is expected to have the form

$$L_1\text{-error} = \alpha N_D^{\beta}. \tag{47}$$

For smooth solution (i.e. continuous differentiable solutions), it is expected that both the RD and FV schemes will exhibit second-order spatial accuracy, i.e. $\beta \approx -2$. For solutions with discontinuities, it is expected that both methods will reduce to first-order spatial accuracy to preserve monotonicity, i.e. $\beta \approx -1$. Where informative, the slope of the line-segment connecting the two finest grids is denoted by β in the error graphs to show the spatial order of accuracy. Of primary interest in Equation (47) is the coefficient α which describes the absolute magnitude of the error. Although of the same formal order of accuracy, it is anticipated that the multidimensional RD schemes will have an error with an absolute magnitude that is lower than that of the FV scheme.

6.1 Performance comparisons for scalar equations

Aside from directly comparing the RD and FV schemes, the effect of grid tessellation is also examined for scalar equations. In each case, a relevant RD distribution scheme was used to compute solutions on grids with an optimal tessellation (diagonal aligned with characteristic vector), a reverse tessellation (diagonal opposite the characteristic vector) and a random unstructured triangular grid.

6.1.1 Linear advection equation

The RD and FV methods are first compared for the linear advection equation given by

$$\frac{\partial u}{\partial t} + a\frac{\partial u}{\partial x} + b\frac{\partial u}{\partial y} = 0, \tag{48}$$

where $a = a(x,y)$ and $b = b(x,y)$ are the components of the advection velocity field. To compare the methods for smooth scalar flows, solutions to a time-invariant problem of circular advection were computed on simple Cartesian grids with uniform spacing. For the circular advection problem, an exponential solution profile, $u = \mathrm{e}^{-0.5[(x-0.5)/0.08]^2}$, is assigned at the $(0 \le x \le 1, y = 0)$ boundary and then advected in a counter-clockwise direction. An interesting aspect of this test case is that the advection velocity is generally not aligned with the Cartesian grid. This challenges the dimensional-splitting of the FV scheme. Because the solution is smooth, the LDA scheme was used to obtain the majorityof the RD results. The LN scheme is also solved to compare its performance relative to the LDA scheme. The FV solution was obtained without using a limiter.

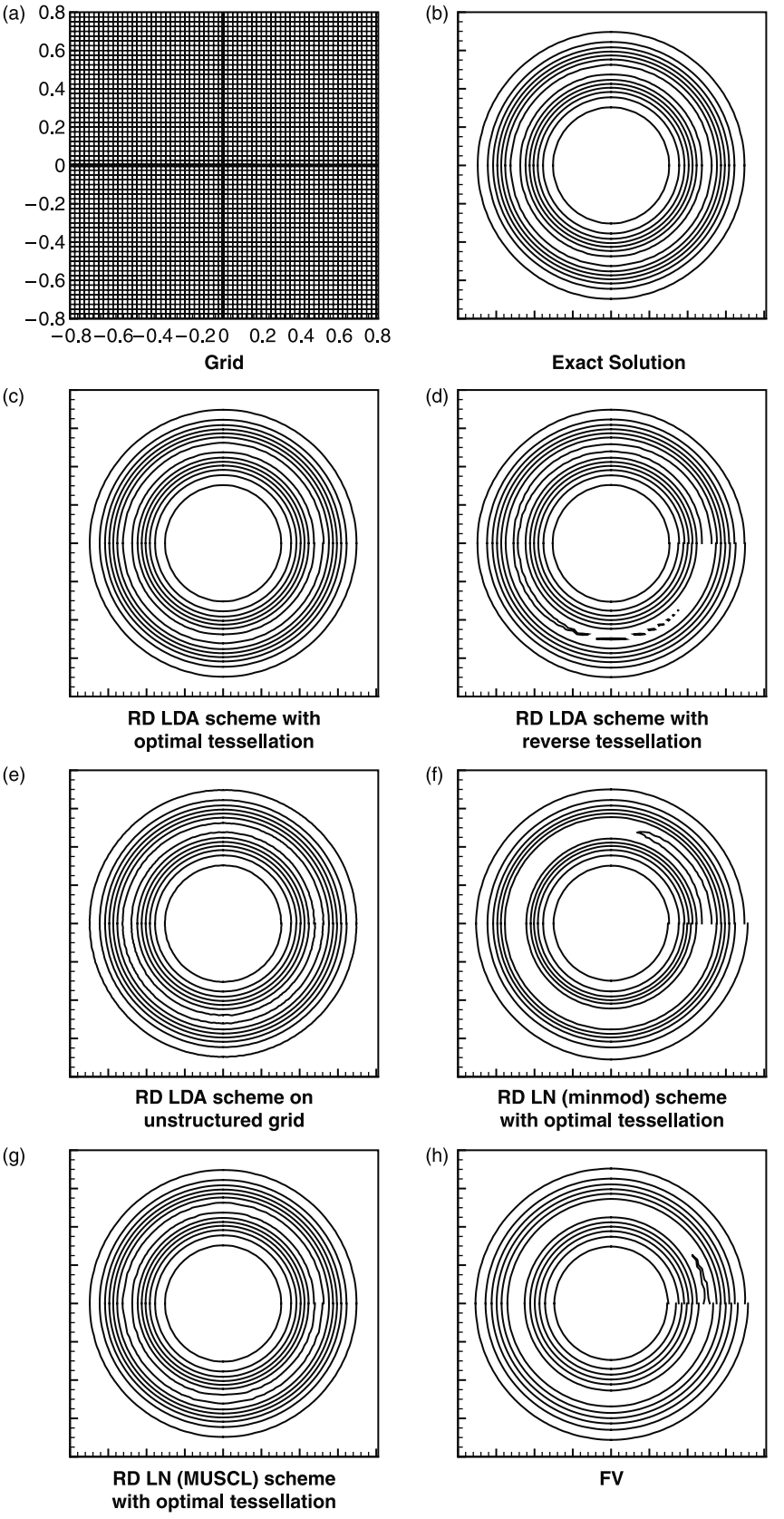

Figure 6. Solutions of circular advection obtained using a 80 × 80 uniform Cartesian mesh.

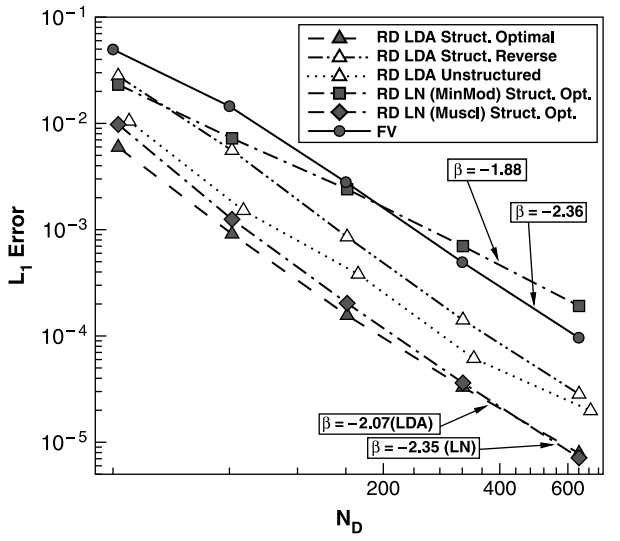

Figure 7. L_1-error as a function of mesh density for circular advection.

However, had one been used, it would have had virtually no effect on the solution. Numerical results were obtained for grid densities ranging from $N_D = 40$ to $N_D = 640$.

Figure 6 shows a Cartesian mesh of size 80 × 80 and the various solutions obtained on that mesh. The grid is shown in Figure 6(a) and a representation of the exact solution on the mesh is shown in Figure 6(b). Notable dissipation is observable in solutions generated by the RD LN (minmod) scheme, FV scheme and RD LDA scheme with a reverse tessellation. Figure 7 depicts the variation of the spatial accuracy with the mesh size.

From the results given in these two figures, it is apparent that the effects of the tessellation are very significant. When using an RD LDA scheme, the optimal tessellation is over half an order of magnitude more accurate that the reverse tessellation. The accuracy achieved on the unstructured grid with the random tessellation lies in between. It is also quite apparent from the predicted errors that, while both the LDA scheme and the FV scheme achieve second-order accuracy for this problem, the absolute error of the LDA scheme with the optimal tessellation is more than an order of magnitude less than that of the FV scheme.

The results for the RD LN scheme with a minmod limiter are somewhat less impressive. Although the LN (minmod) scheme offers a marginal improvement over the FV method on coarser meshes, this quickly disappears because of its lower order-of-accuracy ($\beta \approx -1.88$). As noted in Section 3 the RD LN scheme with a minmod limiter is equivalent to the PSI scheme. The spatial order-of-accuracy can be recovered along with an improvement in the absolute error by instead using a MUSCL limiter (van Leer 1979),

$$\Psi(r) = \max\left[0, \min\left(2r, \frac{r+1}{2}, 2\right)\right]. \qquad (49)$$

The enhanced performance of the MUSCL limiter is thought to be related to the behaviour of the limiter near $r \approx 1$ (Waterson and Deconinck 2007). In the RD framework, the potential benefit of the LN scheme with a MUSCL limiter over the PSI scheme when applied to smooth flows does not appear to have been recognised until now. The effectiveness of the MUSCL limiter is only demonstrated herein for this problem. Elsewhere in this article, results for and discussion of the LN scheme will imply use of the minmod limiter. Finally, note that many other non-linear formulations, such as the blended scheme, also exhibit a similar degraded order of accuracy.

6.1.2 *Non-linear Burgers equation*

The solution to the non-linear Burgers equation, given by

$$\frac{\partial u}{\partial t} + u\frac{\partial u}{\partial x} + 1\frac{\partial u}{\partial y} = 0, \qquad (50)$$

is considered next and used to evaluate the shock-capturing properties of both the RD and FV schemes for scalar equations. A steady problem was studied on a square solution domain in which the boundary values of the solution u was specified to vary linearly from 1.5 to -0.5 along the x-axis at $y = 0$. This results in the formation of a compression wave that strengthens and produces a shock at ($x = 0.75$, $y = 0.5$). The shock then progresses upward and leaves the solution domain to the top right corner. A Cartesian mesh with uniform spacing is again used to obtain the numerical solutions. The compression waves and the shock run at angles to the Cartesian quadrilateral grid, again challenging the dimensional-splitting of the FV scheme. The RD results were obtained using an LN distribution scheme to preserve monotonicity. The FV results used the slope-limiter of Venkatakrishnan (1993) for the same purpose. Numerical results were obtained for grid densities ranging from $N_D = 40$ to $N_D = 640$.

Figure 8 shows the coarsest Cartesian mesh used in the calculations and the various solutions obtained on that mesh. Figure 8(b) depicts a representation of the exact solution on the discrete mesh of Figure 8(a) and numerical solutions obtained using the RD LN scheme with various tessellations are given in Figure 8(c)–(e). The solution obtained using the FV scheme is shown in Figure 8(f). It is evident from these results that, at least

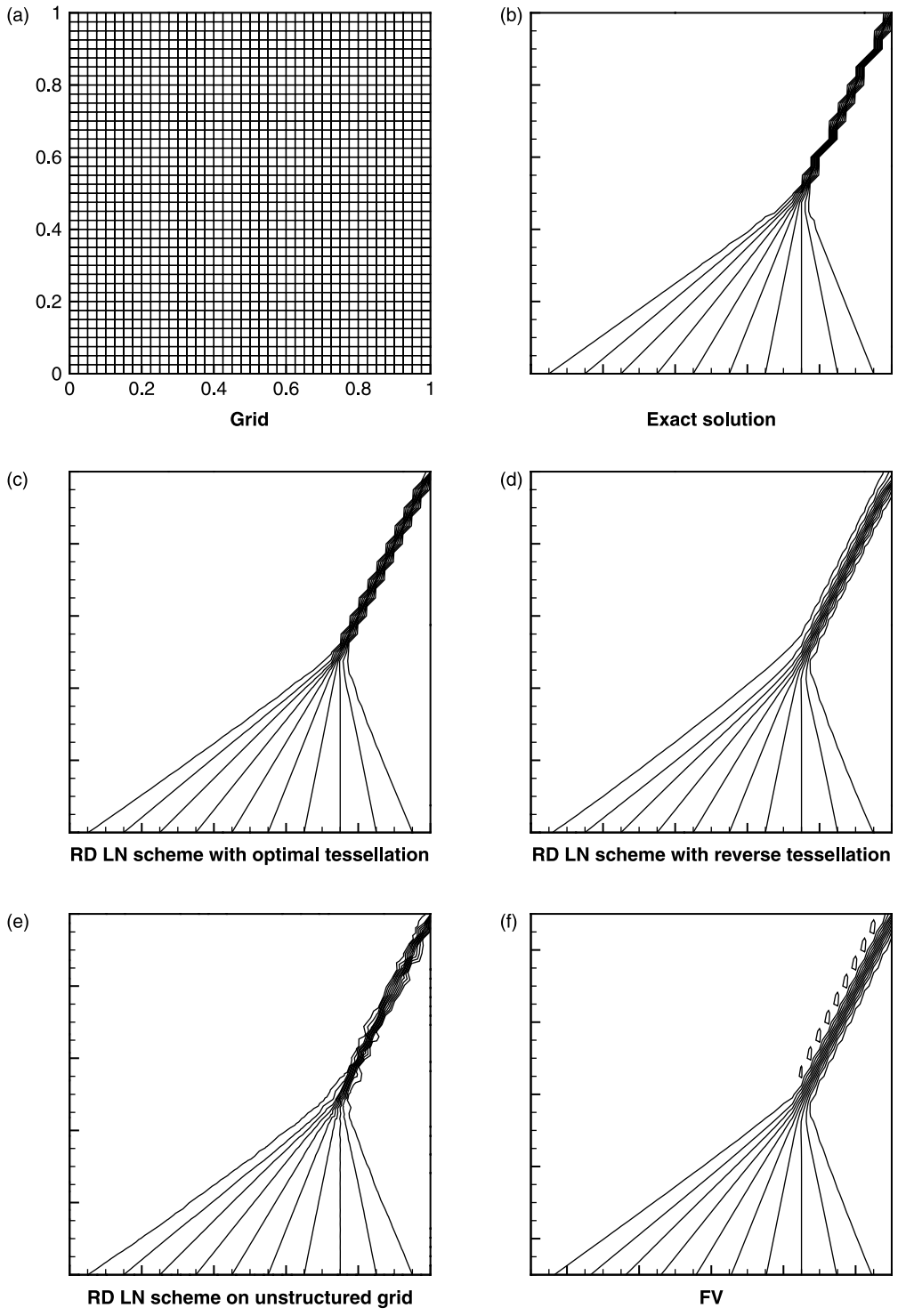

Figure 8. Solutions to Burgers equation obtained using a 40 × 40 uniform Cartesian mesh: (a) grid; (b) exact solution; (c) RD LN scheme with optimal tessellation; (d) RD LN scheme with reverse tessellation; (e) RD LN scheme on unstructured grid; and (f) FV.

qualitatively, the RD LN scheme using an optimal tessellation provides the most compact shock.

Figure 9 depicts the variation of the spatial accuracy with the mesh size. All schemes have near first-order accuracy in the L_1-error norm. The spatial accuracy of the best RD scheme is greater than the FV scheme by more than half an order of magnitude. Interestingly, this is entirely dependent upon proper tessellation of the grid; the RD scheme solved on the reverse tessellation is about equivalent to the FV scheme. As should be expected, the

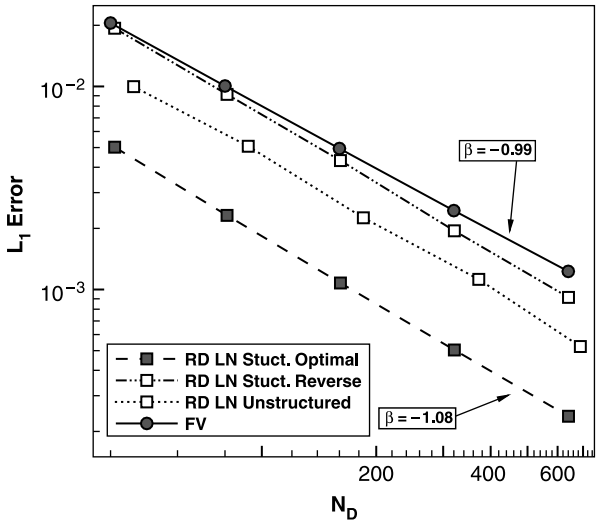

Figure 9. L_1-error as a function of mesh density for Burgers equation.

RD solution on the unstructured mesh is somewhere between the optimal and reverse tessellations.

6.2 *Performance comparisons for the Euler equations*

Steady solutions to the Euler equations are now considered. The performance of the RD and FV schemes are evaluated for a discontinuous supersonic flow, a smooth subsonic flow, a flow with stagnation regions and a smooth transonic flow. Exact solutions are available for all four flows and are used to calculate the spatial accuracy of the methods. The quadrilateral grid used to obtain the RD solutions is always optimally tessellated. For the decomposed RD schemes applied to supersonic flow regimes, a split streamline and dominant acoustic tessellation is used. For the other RD schemes and flow regimes, the tessellation direction is aligned with the flow streamline.

6.2.1 *Supersonic flow past a diamond-shaped aerofoil*

The first problem considered herein related to the Euler equations involves supersonic flow past a diamond-shaped aerofoil with a freestream Mach number of 3, freestream pressure and temperature corresponding to standard atmospheric conditions, and an angle of attack of 0°. The solution domain features a horizontal axis of symmetry and the outflow boundary is close enough to prevent any interaction between the otherwise simple and centred waves. Hence, an exact solution can be determined for the entire domain. Numerical solutions were obtained using a RD decomposed LN scheme (the flow fully decouples everywhere), a RD matrix blended scheme, and, for comparison purposes, the FV scheme. The computationaldomain was divided into four blocks with the body-fitted multiblock grids ranging in size from 160 × 40 to 640 × 160.

Figures 10 and 11 depict both qualitative and quantitative results for the error in the computed density of the RD and FV schemes. Figure 10 shows the coarsest grid used in the accuracy study and the various solutions obtained on that grid for this supersonic flow problem. It is quite apparent from this figure that the numerical shocks obtained with the FV code are somewhat thicker than those of the RD schemes due to its more dissipative nature. The qualitative results for the two RD schemes (decomposed and matrix) appear quite similar. The L_1-norm of the solution error of the various schemes as a function of the mesh size is provided in Figure 11. As expected, all of the schemes exhibit close to first-order accuracy ($\beta = -1$). However, small differences in the absolute error are evident. The decomposed RD solution is the most accurate, followed by the matrix RD solution and then the FV solution.

6.2.2 *Subsonic flow past a smooth bump*

The performance of the RD and FV algorithms is now considered for subsonic flow past a smooth bump. The profile of the bump was defined by

$$y = \frac{1}{20}\left(\cos\left(\frac{\pi x}{1.5}\right) + 1\right), \quad -1.5 \le x \le 1.5. \tag{51}$$

The far-field pressure and temperature were assigned standard atmospheric values and the freestream Mach number was taken to be 0.1. Mach number contours, obtained by the RD decomposed LDA-LW (meaning an LDA distribution for the decoupled scalar equations and Lax–Wendroff distribution for the remaining subsonic acoustic subset) scheme are shown in Figure 12. As this inviscid flow is homentropic, any deviations from the freestream entropy are a result of numerical solution error. Changes in entropy, given by

$$\delta s = \frac{R}{\gamma - 1}\ln\left(\frac{p}{\rho^{\gamma}}\right) - s_{\infty}, \tag{52}$$

were therefore used to define solution error where s_∞ is the value of entropy in the freestream. The computational grid was divided into six blocks and ranges in size from 120 × 80 to 480 × 320. The RD solutions were obtained using a decomposed LDA-LW scheme, a decomposed LN-LW scheme, a matrix LDA scheme, and a matrix blended scheme.

Contours of the entropy change are shown in Figure 13 for solutions obtained on the coarsest mesh. Qualitatively, the decomposed RD schemes show the least entropy production, followed by the matrix RD

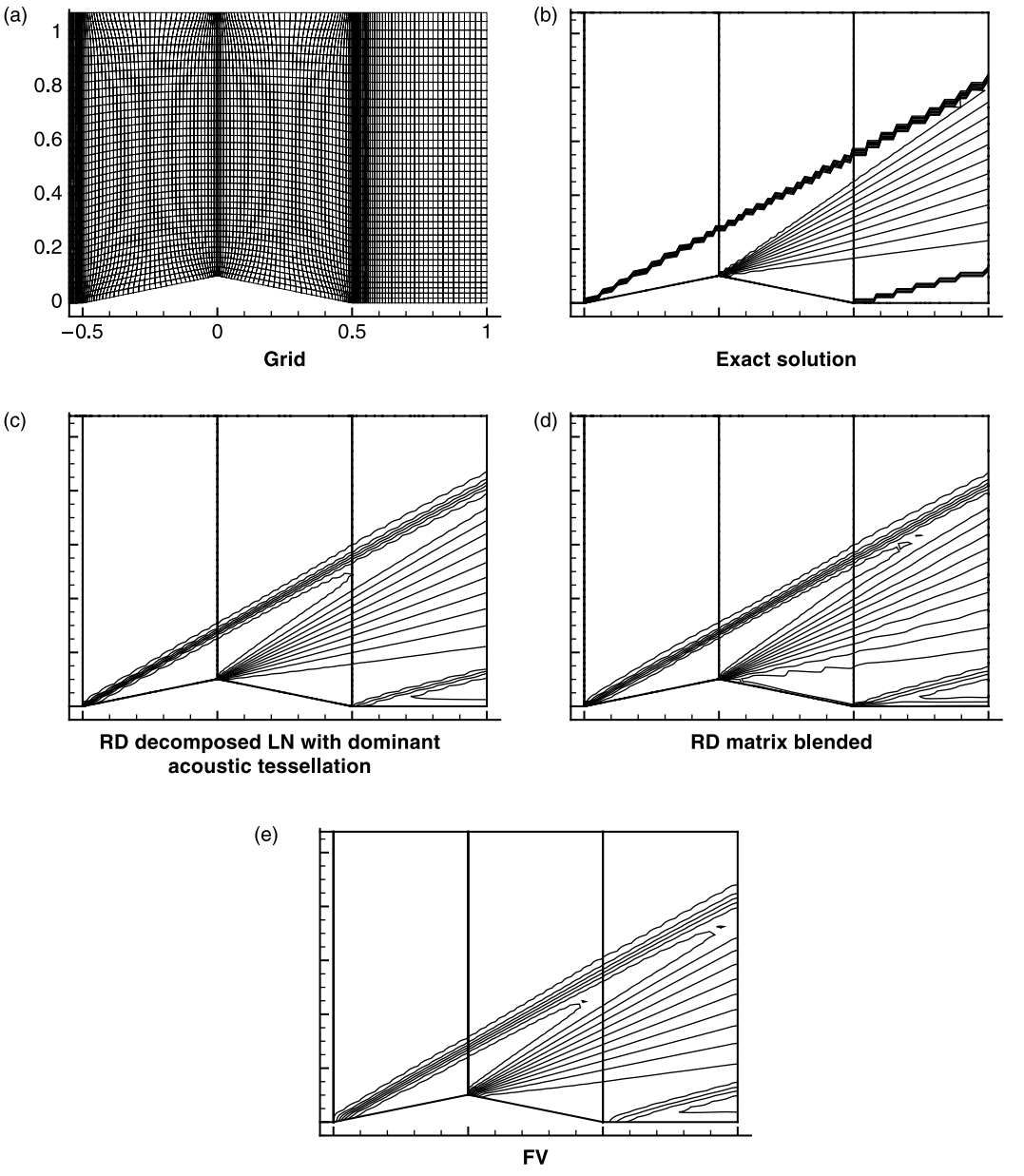

Figure 10. Density distributions for $M = 3$ supersonic flow past a diamond-shaped aerofoil obtained using a 160 × 40 body-fitted multiblock mesh.

schemes and finally, the FV scheme. The spatial convergence is illustrated in Figure 14. The FV scheme and the RD schemes that use an LDA distribution all indicate spatial orders of accuracy near $\beta = -2.64$. The matrix RD schemes perform similarly to the FV scheme. Similar to the performance of the LN (minmod) scheme for scalar equations, the matrix blended scheme shows a degraded order of accuracy compared to the matrix LDA scheme. An interesting result in Figure 14 is that the decomposed RD schemes are much more accurate than the other approaches. The decomposed LDA-LW scheme and the decomposed LN-LW scheme provide nearly identical results, probably because this flow is dominated by the acoustic subsystem. In other words, the results are mostly indicative of how well the subsonic acoustic subset is treated. Experiments revealed that it is the hyperbolic–elliptic splitting, rather than the distribution scheme, that is providing most of the benefit; resolving the acoustic subset with an LDA matrix scheme provides similar results to using the LW scheme.

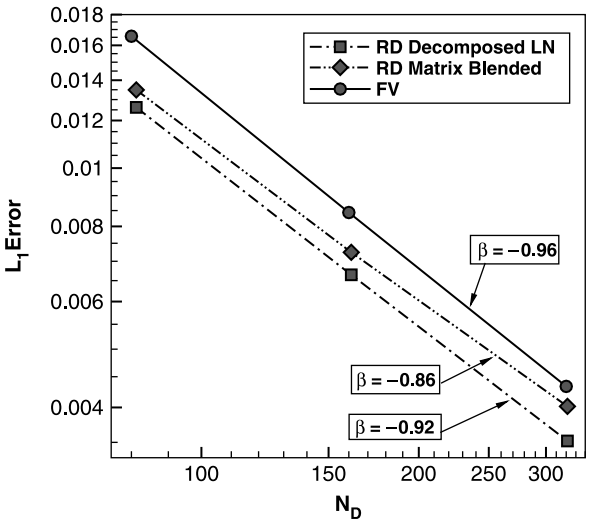

Figure 11. L_1-density-error as a function of grid spacing for $M = 3$ supersonic flow past a diamond-shaped aerofoil.

6.2.3 *Subsonic flow past a circular cylinder*

The more difficult problem of subsonic flow past a circular cylinder was also considered to include the added complexity of stagnation regions. Freestream conditions and error measurements are exactly the same as for the previous case of subsonic flow past a smooth bump. Body-fitted radial grids were used to model the upper half of the cylinder and reflection BCs were applied along the axis of symmetry. As the flow features stagnation regions, system decomposition was not applied in this case due to the degeneracy in the preconditioned system. Numerical solutions were obtained using both matrix LDA and matrix blended RD schemes along with the FV method on multiblock grids ranging from 40 × 40 to 160 × 160 in each quadrant. This is a case where solutions of the RD scheme seem to benefit from using all three nodes in the ghost elements to compute the linearised state (Section 5.2). This modification was made for all RD solutions obtained for this case.

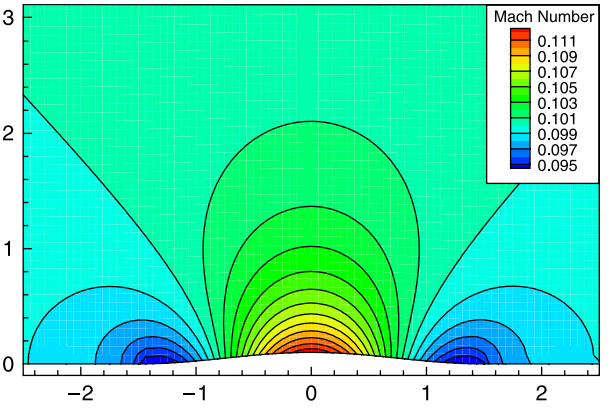

Figure 12. Mach number contours computed by the RD decomposed LDA-LW scheme at $M = 0.1$ (mesh size 240 × 160). (All colour figures available online in colour.)

Contours of the entropy change are shown in Figure 15 for a mesh size of 40 × 40 in each quadrant. From this figure, it should be quite evident that the RD LDA scheme produces much less entropy than the FV scheme. Qualitatively at least, the RD schemes provide a significantly improved result as compared to the FV method. Naturally, even greater improvements would be expected if the decomposed RD scheme could have been used. Quantitative comparisons of the methods are given by the variation of the solution accuracy with respect to mesh density as shown in Figure 16. The results depicted in the figure are somewhat peculiar and not quite as expected. Although the curve of FV error is virtually a straight line, it indicates a spatial order of accuracy of 2.79. This is higher than the expected value of 2. On the other hand, the RD blended scheme initially shows an order of accuracy of 1.88, a value that agrees very well with the scalar RD LN (minmod) results in Figure 7. However, on finer grids, the accuracy degrades to an order of 1.29. The behaviour of the solution error for the LDA scheme, although generally much lower than that of the FV method (at least for the coarser meshes) and having an order of accuracy that approaches 2.5, is erratic and also not as expected. Although it could be argued that the asymptotic regime for the solution error in terms of the mesh resolution has not yet been achieved on the range of grids considered, this explanation is not supported by the FV results, for which asymptotic-like behaviour is observed. Instead, a cause for the behaviour of the RD LDA scheme may be some form of numerical instability. This instability is especially noticeable on the finer meshes.

Figure 17 shows the predicted Mach number and entropy distributions on a grid with 80 × 80 cells in each quadrant. This solution was obtained using the LDA scheme. The L_2 norm for all solution residuals was reduced by 15 orders of magnitude indicating that a steady solution was indeed achieved. Although the Mach number contours are smooth and symmetrical, the entropy solution displays a number of perturbations. Similar, but less significant, perturbations were also observed in the blended results. The oscillations seem to be highly sensitive to the grid. A pre-defined tessellation can exacerbate the situation. Letting the tessellation optimally adapt to the solution tends to minimise the oscillations. An unstructured mesh disrupts the regularity of the perturbations, but their effect is still otherwise present. To our knowledge, this behaviour has not been reported elsewhere in the literature. There has been some

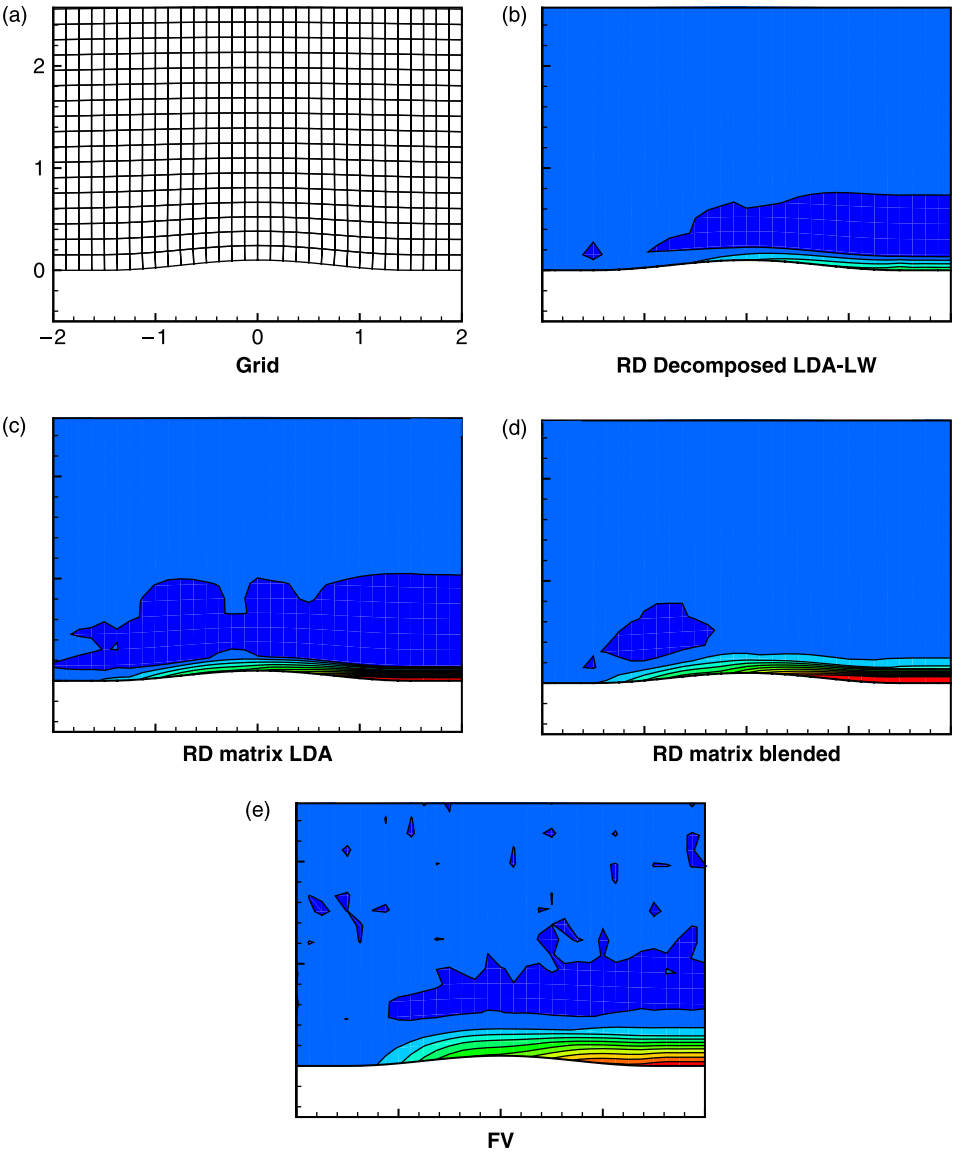

Figure 13. Distributions of entropy change for $M = 0.1$ subsonic flow past a smooth bump (mesh size 120 × 80).

recent efforts to correct curiously similar perturbations in smooth regions (Abgrall 2006, Dobeš and Deconinck in press); however, these efforts only acknowledge instabilities for non-linear distribution schemes.

6.2.4 *Ringleb's flow*

Ringleb's flow is a hodograph solution to the Euler equations (Sachdev *et al.* 2005) that involves an isentropic and irrotational flow contained between two streamlines. The availability of the analytic solution for this case make it very useful for demonstrating the accuracy of the spatial discretisation. Figure 18(c),(d) show the Mach number and density distributions corresponding to the exact solution. The left and right boundaries are delimited by streamlines and and there is subsonic inflow at the top and mixed subsonic/supersonic outflow at the bottom of the domain. Numerical solutions were obtained for Ringleb's flow using both the RD and FV schemes on body fitted grids ranging in size from 40 × 40 to 320 × 320. An example grid, coarser than the coarsest grid solved and shown for illustrative purposes only, is displayed in Figure 18(a). The RD solutions were obtained using a matrix LDA scheme, a matrix blended scheme, a decomposed LDA scheme and a decomposed LN scheme. In subsonic regions, the elliptic acoustic subset of the decomposed Euler equations was solved using the Lax–Wendroff approach described previously.

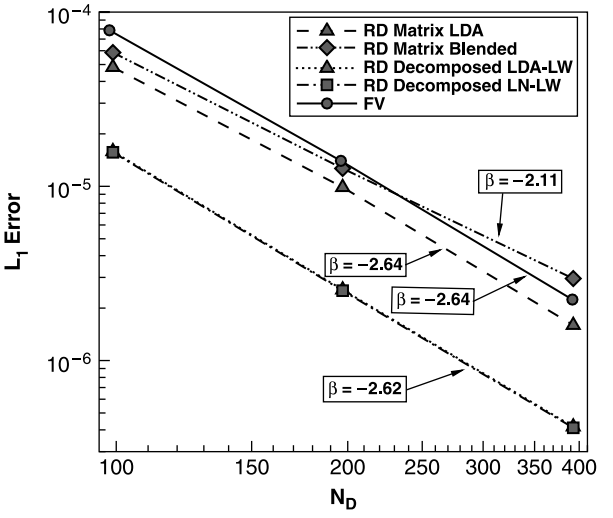

Figure 14. L_1-error as a function of grid density for $M = 0.1$ subsonic flow past a smooth bump.

The blending coefficient or limiter of the non-linear RD schemes was frozen when the solution was fully developed. In the previous problems, freezing the limiter would avoid a convergence stall but not appreciably influence the overall accuracy of the results. It was therefore not used. For this problem, freezing the limiter and extending the convergence did actually lead to more accurate estimations of the solution accuracy of the non-linear RD schemes.

The L_1-error norms of the computed difference in the solution densities are shown in Figure 19 for the Ringleb's flow problem. The results indicate that the FV and both of the RD LDA schemes have spatial orders of accuracy near 2, as should be expected. However, in this case, it is the FV scheme that yields the best results, providing solutions that appear to be almost twice as accurate as the decomposed LDA scheme. The performance of the non-linear RD schemes is inferior to that of the linear LDA schemes. For the matrix blended method, a degradation in the order of accuracy is seen on finer grids, similar to that observed for flow past a cylinder. Between the two finest meshes, the order of accuracy is only -1.24. On the finest mesh, 320×320, the decomposed LN method produced oscillations that severely corrupt the accuracy. However, the decomposed LN results that were obtained seem to follow a trend similar to that of the matrix blended results. As with the supersonic case, the decomposed RD schemes show a slight improvement in absolute accuracy over the RD matrix schemes.

The discrepancy regarding the relative accuracies of RD and FV methods is known to not be related to mesh

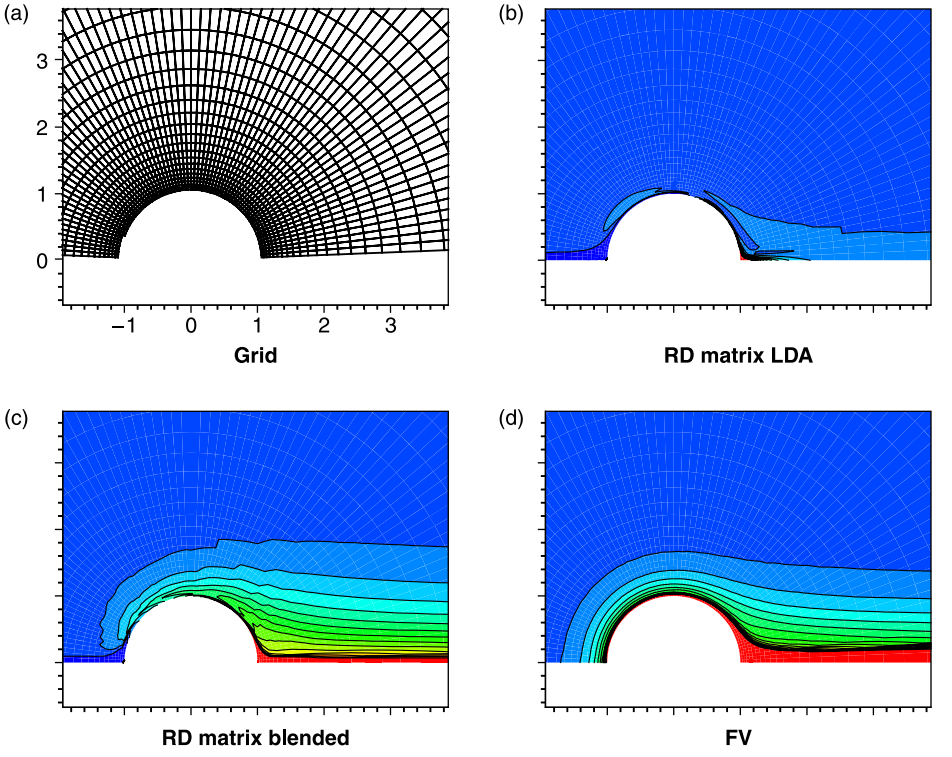

Figure 15. Distributions of entropy change for $M = 0.1$ subsonic flow past a circular cylinder (mesh size 40×40 in each quadrant).

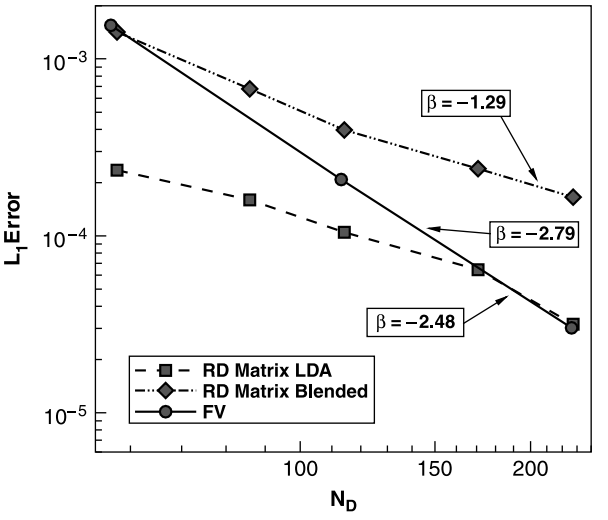

Figure 16. L_1-error as a function of grid density for $M = 0.1$ subsonic flow past a circular cylinder.

alignment. This was proven by generating solutions on randomly distorted grids, similar to that shown in Figure 18(b). For this grid, a limiter was not used to obtain the FV solution (use of the limiter on the smooth grid had virtually no effect on the results). The results for the unlimited FV method are compared to those for the matrix-LDA RD scheme on the distorted mesh in Figure 19. It should be evident from this figure that while second-order accuracy is still achieved on the distorted grids, there is a notable decrease in the solution accuracy of both methods. However, the overall effect on each of the methods is quite similar such that the FV scheme is still more accurate than the RD scheme.

The discrepancy is thought to be related to how well the schemes correct solutions in regions that violate the entropy condition. Entropy violations result from the discretisation and typically occur when a node receives no update because all waves move away from the node. This commonly occurs at sonic points and, in some cases, can create a expansion shocks. Figure 20(a),(b) show the absolute magnitude of the density error for the FV and RD schemes, respectively. It is apparent that the RD scheme suffers from higher error levels near sonic points. The entropy fix proposed by Sermeus and Deconinck (2005) was implemented for the matrix scheme. Regions where an entropy fix may be required, as detected by this scheme, are shown in Figure 20(c). The effect of applying the entropy fix is displayed in Figure 20(d). Although almost indistinguishable from Figure 20(b), there is a small improvement to the accuracy[1]. Most of the improvement is at the large error in the centre of the domain. The large error at the outflow boundary is caused by an entropy violation within the degenerate ghost elements and is not dealt with at all by the entropy fix.

The FV scheme is more accurate than the RD scheme even when an entropy fix is applied. It seems likely that the results reported in Figure 19 are more indicative of how well the two schemes satisfy the appropriate entropy condition than anything else. The FV method is much more successful, probably because of its larger stencil. In one dimension, a second-order reconstruction will tend to remove most entropy violations. The RD scheme, on the other hand, must completely rely on accurate multi-dimensional analytical approximations of the solution in regions of entropy violation. Besides the entropy correction considered here, fixes have also been proposed by Wood and Kleb (2001) and Nishikawa and Roe (2005).

7. Conclusions

The intent of this study was to quantitatively assess the benefits to solution accuracy offered by RD schemes as compared to more standard FV methods for problems involving both discontinuous and smooth solutions.

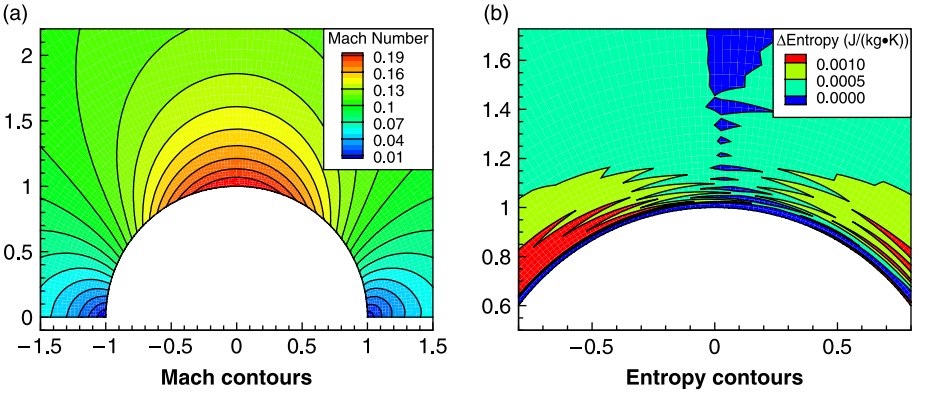

Figure 17. Perturbations in the subsonic cylinder flow generated by the RD LDA scheme (mesh size 80 × 80 in each quadrant).

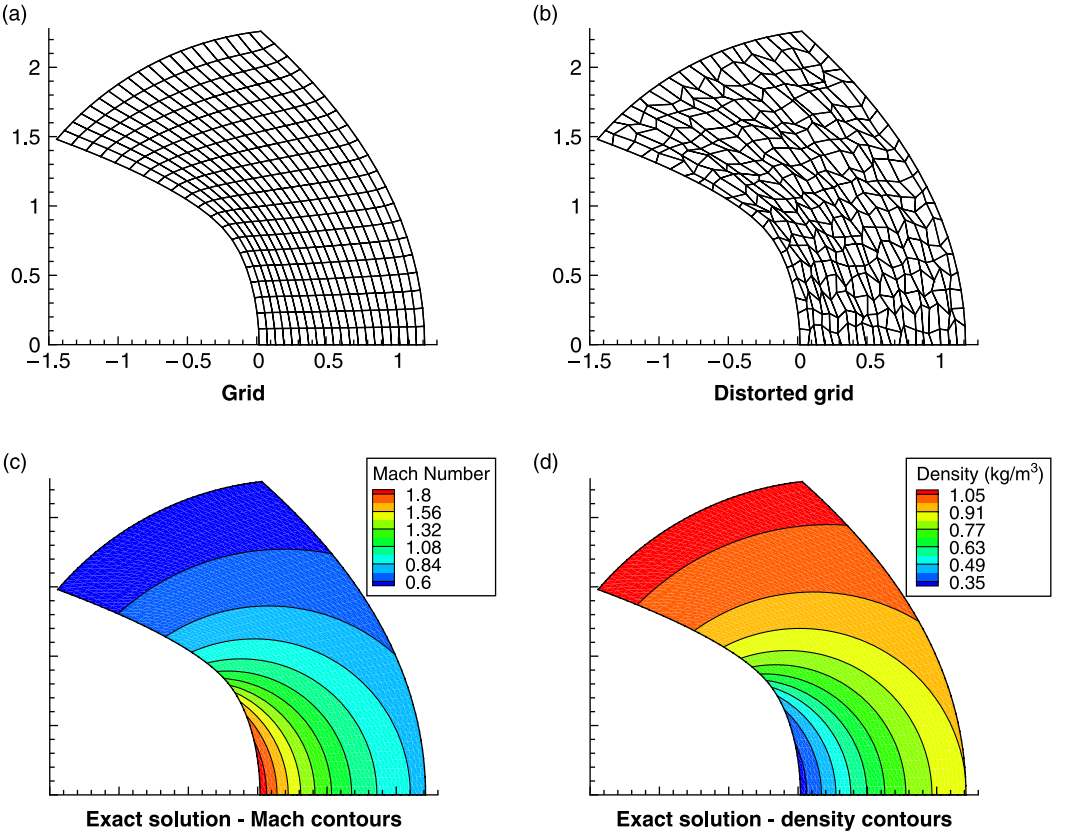

Figure 18. Contours of the exact solution for Ringleb's flow.

Although originally developed for unstructured grids, use of an RD scheme on a structured quadrilateral mesh permits optimal solution-dependent tessellation of the domain. The scalar results demonstrate significant improvements in accuracy from the optimal tessellation procedure.

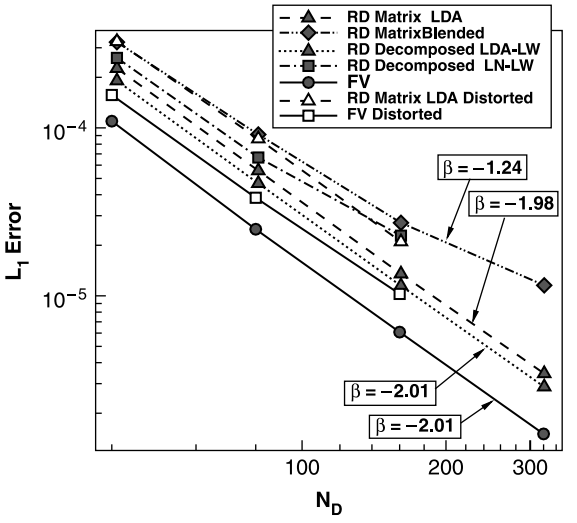

Figure 19. L_1-density-error as a function of grid density for Ringleb's flow.

The numerical results presented here for scalar partial differential equations indicate that the RD method is far superior to the FV method, both in smooth regions and in the presence of discontinuities and/or shocks. Significant improvements in accuracy can be achieved for the same mesh resolution. Unfortunately, while the LN scheme with a minmod limiter (equivalent to the PSI scheme) is excellent at capturing discontinuities, it suffers a degradation in the spatial accuracy as compared to the LDA scheme when applied to problems having smooth flows. Second-order accuracy is not achieved for smooth solutions using the LN (minmod) and blended distribution schemes. The deficiency appears to be related to the performance of the limiter in smooth regions. Solutions of smooth scalar problems computed by an LN scheme with a MUSCL limiter display an accuracy similar to that achieved with the LDA scheme. Further work is required to examine the effect of the MUSCL limiter on discontinuous problems and to extend the benefits to systems of equations. Other possible fixes include defining blending coefficients that are based on the

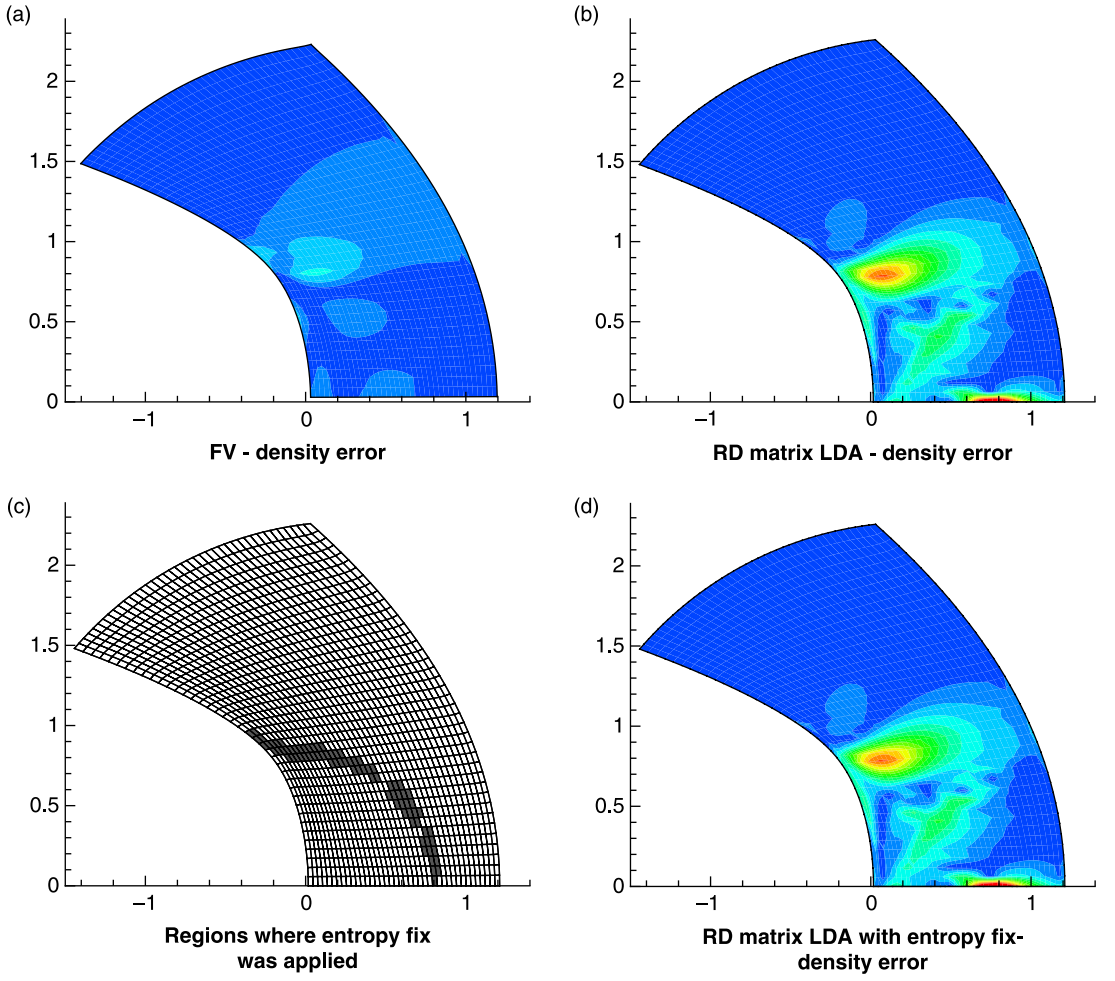

Figure 20. Distributions of the density error generated by the RD and FV schemes and performance of an entropy fix.

explicit detection of discontinuities (Dobeš and Deconinck in press).

Various extensions of the RD scheme to systems of partial differential equations have also been described and the numerical results for supersonic flow solutions to the Euler equations appear to support the results and conclusions obtained for the scalar equations. The RD scheme was also quite successful at resolving subsonic flow over a smooth bump with the decomposed scheme demonstrating exceptional performance. However, difficulties were encountered for the cases of subsonic flow past a cylinder and transonic Ringleb's flow. Although RD solutions for the subsonic cylinder flows are generally found to be superior to those provided by the FV method, the graphs of the solution error do not fully support this finding. Furthermore, close examination of the numerical results reveals perturbations and/or instabilities in the solutions, something unexpected for an LDA scheme applied to smooth flows. For Ringleb's flow, the computed results somewhat surprisingly reveal that the FV scheme is more accurate. A probable explanation is that the RD scheme has more difficulty providing an entropy satisfying solution near sonic points of expanding flows. This is likely a byproduct of the smaller stencil and possibly the linearisation process.

Overall, the RD method appears quite promising as an alternative to FV methods. The performance of the method for the scalar equations alone motivates further research. However, it would seem that the accuracy of the standard non-linear distribution schemes and the reliability of the distribution techniques for non-linear systems of equations must be improved before the RD method is as practical and robust as FV methods for a wide range of applications.

Acknowledgements

The first author would like to acknowledge the financial support received from the Ontario government in the form of an Ontario Graduate Scholarship.

Note

1. Improvements are more noticeable when expansion shocks are actually visible.

References

Abgrall, R., 2001. Toward the ultimate conservative scheme: following the quest. *Journal of Computational Physics*, 167, 277–315.

Abgrall, R., 2006. Essentially non-oscillatory residual distribution schemes for hyperbolic problems. *Journal of Computational Physics*, 214, 773–808.

Abgrall, R. and Mezine, M., 2004. Construction of second-order accurate monotone and stable residual distribution schemes for steady problems. *Journal of Computational Physics*, 195, 474–507.

Abgrall, R. and Roe, P.L., 2003. High order fluctuation schemes on triangular meshes. *Journal of Scientific Computing*, 19 (1–3), 3–36.

Csík, A., Ricchiuto, M. and Deconinck, H., 2002. A conservative formulation of the multidimensional upwind residual distribution schemes for general nonlinear conservation laws. *Journal of Computational Physics*, 179, 286–312.

Deconinck, H., Powell, K.G., Roe, P.L. and Struijs, R., 1991. Multi-dimensional schemes for scalar advection. *AIAA CFD conference*, AIAA paper 91-1532.

Deconinck, H., Sermeus, K. and Abgrall, R., 2000. Status of multidimensional upwind residual distribution schemes and applications in aeronautics. *AIAA fluids conference*, AIAA paper 2000-2328.

Dobeš, J. and Deconinck, H., in press. Second order blended multidimensional upwind residual distribution scheme for steady and unsteady computations. *Journal of Computational and Applied Mathematics*.

Godunov, S.K., 1959. Finite-difference method for numerical computations of discontinuous solutions of the equations of fluid dynamics. *Matematicheskii Sbornik*, 47, 271–306.

Gottlieb, J.J. and Groth, C.P.T., 1988. Assessment of riemann solvers for unsteady one-dimensional inviscid flows of perfect gases. *Journal of Computational Physics*, 78, 437–458.

Mesaros, L.M., 1995. *Multi-dimensional fluctuation splitting schemes for the Euler equations on unstructured grids*. Thesis (PhD). University of Michigan.

Nishikawa, H. and Roe, P.L., 2005. Adaptive-quadrature fluctuation-splitting schemes for the Euler equations. *AIAA CFD Conference*, AIAA paper 2005-4865.

Paillère, H., 1995. *Multidimensional upwind residual distribution schemes for the Euler and Navier–Stokes equations on unstructured grids*. Thesis (PhD). Université Libre de Bruxelles.

Rad, M., 2001. *A residual distribution approach to the Euler equations that preserves potential flow*, Thesis (PhD). University of Michigan.

Roe, P.L. and Sidilkover, D., 1992. Optimum positive linear schemes for advection in two and three dimensions. *SIAM Journal of Numerical Analysis*, 29 (6), 1542–1568.

Sachdev, J.S., Groth, C.P.T. and Gottlieb, J.J., 2005. A parallel solution-adaptive scheme for predicting multi-phase core flows in solid propellant rocket motors. *International Journal of Computational Fluid Dynamics*, 19 (2), 157–175.

Sermeus, K. and Deconinck, H., 2005. An entropy fix for multi-dimensional upwind residual distribution schemes. *Computers and Fluids*, 34, 617–640.

Sidilkover, D. and Roe, P.L., 1995. *Unification of some advection schemes in two dimensions*. ICASE, Technical Report 95-10.

Struijs, R., 1994. *A multi-dimensional upwind discretization method for the Euler equations on unstructured grids*. Thesis (PhD). Technische Universiteit Delft.

van Leer, B., 1979. Towards the ultimate conservative difference scheme. V. A second-order sequel to Godunov's method. *Journal of Computational Physics*, 32, 101–136.

van der Weide, E., Deconinck, H., Issman, E. and Degrez, G., 1999. A parallel, implicit, multi-dimensional upwind, residual distribution method for the Navier–Stokes equations on unstructured grids. *Computational Mechanics*, 23, 199–208.

Venkatakrishnan, V., 1993. On the accuracy of limiters and convergence to steady state solutions. AIAA paper 93-0880.

Waterson, N.P. and Deconinck, H., 2007. Design principles for bounded higher-order convection schemes – a unified approach. *Journal of Computational Physics*, 224, 182–207.

Wood, W.A., 2001. *Multi-dimensional upwind fluctuation splitting scheme with mesh adaption for hypersonic viscous flow.* Thesis (PhD). Virginia Polytechnic Institute and State University.

Wood, W.A. and Kleb, W.L., 1999. Diffusion characteristic of finite volume and fluctuation splitting schemes. *Journal of Computational Physics*, 153, 353–377.

Wood, W.A. and Kleb, W.L., 2001. 2-D/Axisymmetric formulation of multi-dimensional upwind scheme. *15th AIAA CFD conference*, AIAA paper 2001-2630.